NASA-CR-198983

P-49

ORIGINAL CONTAINS
COLOR ILLUSTRATIONS

7

MCAT Institute
Final Report
NCC2-698-95-12

Boundary Layer Transition Studies

Jonathan H. Watmuff

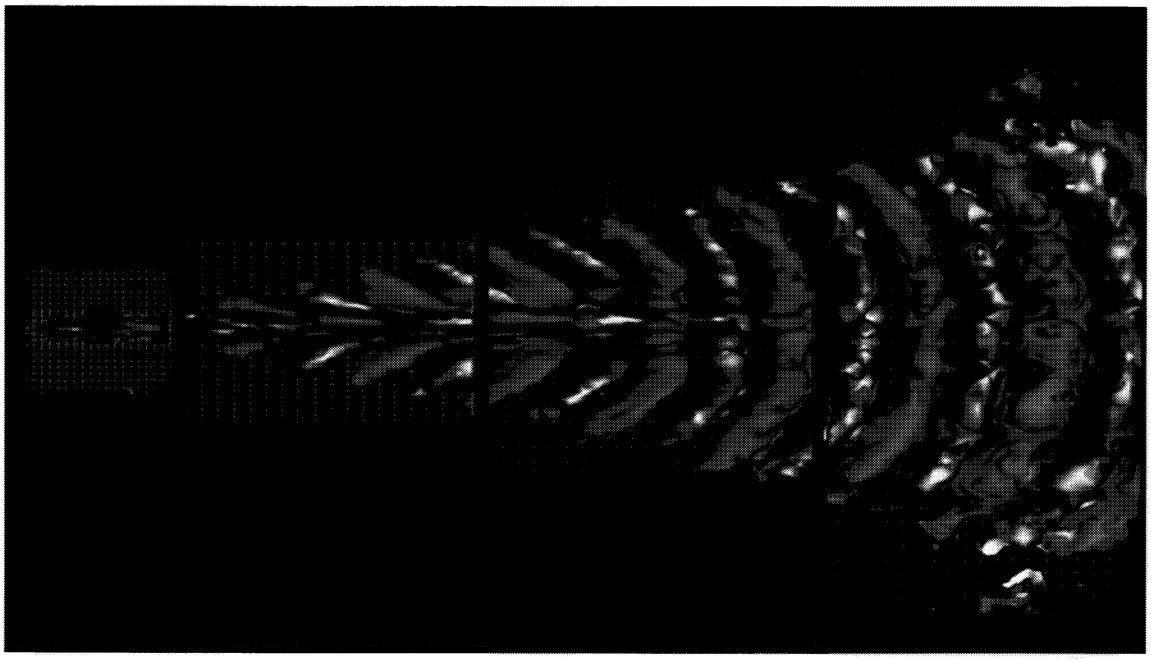

February 1995

MCAT Institute
3933 Blue Gum Drive
San Jose, CA 95127

(NASA-CR-198983) BOUNDARY LAYER TRANSITION STUDIES Final Report, Nov. 1990 - Feb. 1995 (MCAT Inst.) 49 p

N95-32454

Unclas

G3 /34 0059133

MCAT Institute Final Report NCC2-698-95-12

Boundary Layer Transition Studies

Dr. Jonathan H. Watmuff

Cooperative Agreement NCC2-698

November 1990 to February 1995

Mailing Address:

Dr. Jonathan H. Watmuff
M/S 260-1
NASA Ames Research Center
Moffett Field, CA 94305

MCAT Institute
3933 Blue Gum Drive
San Jose, CA 95127

ABSTRACT

A small-scale wind tunnel previously used for turbulent boundary layer experiments was modified for two sets of boundary layer transition studies. The first study concerns a laminar separation/turbulent reattachment. The pressure gradient and unit Reynolds number are the same as the fully turbulent flow of Spalart and Watmuff (1993). Without the trip wire, a laminar layer asymptotes to a Falkner & Skan similarity solution in the FPG. Application of the APG causes the layer to separate and a highly turbulent and approximately 2D mean flow reattachment occurs downstream. In an effort to gain some physical insight into the flow processes a small impulsive disturbance was introduced at the C_p minimum. The facility is totally automated and phase-averaged data are measured on a point-by-point basis using unprecedently large grids. The evolution of the disturbance has been tracked all the way into the reattachment region and beyond into the fully turbulent boundary layer. At first, the amplitude decays exponentially with streamwise distance in the APG region, where the layer remains attached i.e. the layer is viscously stable. After separation, the rate of decay slows, and a point of minimum amplitude is reached where the contours of the wave packet exhibit dispersive characteristics. From this point, exponential growth of the amplitude of the disturbance is observed in the detached shear layer i.e. the dominant instability mechanism is inviscid. A group of large-scale 3D vortex loops emerges in the vicinity of the reattachment. Remarkably, the second loop retains its identity far downstream in the turbulent boundary layer. The results provide a level of detail usually associated with CFD.

Substantial modifications were made to the facility for the second study concerning disturbances generated by Suction Holes for Laminar Flow Control (LFC). The test section incorporates suction through interchangeable porous test surfaces. Detailed studies have been made using isolated holes in the impervious test plate that was used to establish the Blasius base flow. The suction is perturbed harmonically and data are averaged on the basis of the phase of the disturbance, for conditions corresponding to strong suction and without suction. The technique was enhanced by using up to nine multiple probes to reduce the experimental run-time. In both cases, 3D contour surfaces in the vicinity of the hole show highly 3D TS waves which fan out in the spanwise direction forming bow-shaped waves downstream. The case without suction has proved useful for evaluating calculation methods. With suction, the perturbations on the centerline are much stronger and decay less rapidly, while the TS waves in the far field are similar to the case without suction. Downstream, the contour surfaces of the TS waves develop spanwise irregularities which eventually form into clumps. The spanwise clumping is evidence of a secondary instability that could be associated with suction vortices. Designers of porous surfaces use Goldsmith's Criterion to minimize cross-stream interaction. However nothing is known about the streamwise interactions. It is shown that partial TS wave cancellation is possible, depending on the hole spacing, disturbance frequency and free-stream velocity.

New high-performance Constant Temperature Hot-Wire Anemometers were designed and built, based on a linear system theory analysis that can be extended to arbitrary order. The motivation was to achieve the highest possible frequency response while ensuring overall system stability. The performance is equal to or superior to commercially available instruments at about 10% of the cost. Details, such as fabrication drawings and a parts list, have been published to enable the instrument to be constructed by others.

TABLE OF CONTENTS

NOMENCLATURE

Abbreviations:

ADC	Analog to Digital Converter
APG	Adverse Pressure Gradient
CFD	Computational Fluid Dynamics
CI	Contour Increment i.e. stepsize between successive contours
DNS	Direct Numerical Simulation
FPG	Favorable Pressure Gradient
LFC	Laminar Flow Control
LST	Linear Stability Theory
PSE	Parabolized Stability Equations
TS	Tolmien-Schlichting (as in TS waves)
ZPG	Zero Pressure Gradient

Symbol:

C_p	pressure coefficient (dimensionless)
C_q	suction coefficient ($=V/U$), (dimensionless)
f	frequency (Hz)
F	frequency ($=2\pi f\nu/U_\infty^2$), (dimensionless)
H	shape factor (dimensionless)
m	exponent of power law for free-stream velocity variation (Falkner & Skan)
S	separation parameter, $= (\theta^2_{sep}/\nu)\ (\partial U/\partial x)_{sep}$ (dimensionless)
U	velocity in the x-direction along the test plate (m/s)
u	fluctuating component of U (m/s)
V	bulk suction velocity through the test plate (m/s)
(x, y, z)	coordinate system: (m) origin for Laminar Separation/Turbulent Reattachment study is Contraction Exit origin for Suction Hole Study is leading edge of test plate

Greek Symbols:

β	Falkner & Skan wedge angle (also turbulent boundary layer PG parameter)
ϕ	phase (64 phase intervals are used for all measurements)
ν	viscosity (m^2/s)
θ	momentum thickness (mm)
λ	shear layer velocity ratio (dimensionless)
ω^*	dominant frequency of instability for shear layer (dimensionless)

Subscripts:

x	coordinate e.g. Re_x, Reynolds number based on x
ref	reference condition
ϕ	phase-averaged quantity
rms	root mean square quantity
max	maximum quantity
∞	free-stream value

Units: SI units are used (approximate English units are given in parentheses)

EXTENDED SUMMARY

A small-scale wind tunnel previously used for turbulent boundary layer experiments was modified for two sets of boundary layer transition studies: (1) Laminar Separation/Turbulent Reattachment, and (2) Disturbances Generated by Suction Holes for Laminar Flow Control. Another subtask consisted of the design and fabrication of High-performance Constant Temperature Hot-Wire Anemometers. Twenty-eight instruments are currently in use within the Fluid Mechanics Laboratory.

1. Laminar Separation / Turbulent Reattachment

The first set of experiments consisted of simply removing the trip wire used for the combined numerical and experimental study of a turbulent boundary layer developing in an adverse pressure gradient (Spalart and Watmuff 1993). A Favorable Pressure Gradient (FPG) is first applied and the layer asymptotes to the Falkner & Skan similarity solution based on the local pressure gradient. Flying hot-wire measurements are used to determine the salient features of a thin separation bubble that forms in the Adverse Pressure Gradient (APG). A highly turbulent, but 2D mean flow reattachment occurs about 0.2m (8 inches) downstream of the separation and the flying hot-wire data has been used to identify the regions where large rectification errors occur in the stationary probe data. The properties of the turbulent boundary layer downstream of the reattachment are markedly different from the flow of Spalart and Watmuff e.g. the skin friction is almost double.

In an effort to gain some physical insight into the flow processes a small impulsive disturbance was repetitively introduced through a small pressure tapping at the C_p minimum. The facility is totally automated under computer control and can be run continuously (24 hours/day) for weeks at a time. Phase-averaged data is collected on a point-by-point basis on unprecedently large spatially dense grids. The high spatial resolution of the data provides a level of detail that is usually associated with CFD.

The evolution of the disturbance has been tracked all the way into the reattachment region and beyond into the fully turbulent boundary layer. Initially, the layer is attached and the maximum amplitude of the generated wave packet decays exponentially with streamwise distance. Pseudo-flow visualization contours of the wave packet show that it maintains much the same shape and form. These observations provide evidence indicating that the layer is viscously stable. After separation, the rate of decay slows and a point of minimum amplitude is reached where the amplitude contours of the wave packet have developed dispersive characteristics. A region of exponential growth rate follows and the dispersive wave packet follows a trajectory corresponding to the inflection points in the mean flow i.e. the dominant instability mechanism is inviscid. Further evidence for this assertion is observed in the region leading up to and including the reattachment which was measured with cross-wires. Contour surfaces of phase-averaged vorticity calculated from the data clearly show the presence of a Kelvin-Helmholtz type of instability in the detached shear layer. Beyond this point the growth becomes nonlinear and a group of large-scale 3D vortex loops emerges in the vicinity of the reattachment. Remarkably, the second dominant loop retains its identity far downstream in the fully turbulent boundary layer.

Accurate calculation of this flow is currently beyond the capabilities of CFD yet a simple Falkner & Skan similarity solution could be used as the inlet boundary condition for a corresponding CFD study. Therefore the measurements will act as a useful database for advanced code development.

2. Disturbances Generated by Suction Holes for Laminar Flow Control.

For the next set of experiments substantial modifications were made to the facility to conduct investigations into the use of suction as a means of Laminar Flow Control (LFC). The test section has been modified to incorporate suction through interchangeable porous test surfaces and a Zero Pressure Gradient (ZPG) is used to establish the (Blasius) base flow. A 20:1 scale porous test surface has been machined for improved spatial resolution with hot wires. Substantial enhancements were also made to the 3D probe traverse and experimental technique. For example, multiple probes have been incorporated to extend size of the measurement grids without incurring an increase in experimental run-time.

Detailed studies have been made to explore the underlying instability mechanisms using isolated holes in the impervious test plate that was used to establish the Blasius base flow. The suction is perturbed harmonically and data are averaged on the basis of the phase of the disturbance. Conditions corresponding to strong suction and without suction have been studied. In both cases, 3D contour surfaces in the vicinity of the hole show highly 3D Tolmien-Schlichting (TS) waves which fan out in the spanwise direction leading to bow-shaped waves downstream. For the case without suction, the data was compared with Linear Stability Theory (LST), Parabolized Stability Equations (PSE) and Direct Numerical Simulation (DNS) calculations, see Mack and Herbert (1995). Only the DNS was able to generate a disturbance field similar to the measurements in the vicinity of the hole. With suction, the perturbations on the centerline are much stronger and decay less rapidly, while the TS waves in the far field are similar to the case without suction. Downstream, the contour surfaces of the bow-shaped TS waves develop spanwise irregularities which eventually form into clumps. The contours remain smooth when suction is not applied. The spanwise clumping is evidence of a secondary instability that could be associated with suction hole vortices.

Designers of porous surfaces use Goldsmith's Criterion to minimize cross-stream interaction between suction hole vortices. However nothing is known about the streamwise interactions. It is shown that partial TS wave cancellation is possible, depending on the hole spacing, disturbance frequency and free-stream velocity.

3. High-performance Constant Temperature Hot-Wire Anemometers.

New high-performance Constant Temperature Hot-Wire Anemometers were designed and built, based on a linear system theory analysis that can be extended to arbitrary order. The motivation was to achieve the highest possible frequency response while ensuring overall system stability. The performance is equal to or superior to commercially available instruments at about 10% of the cost. Details, such as fabrication drawings and a parts list, have been published to enable the instrument to be constructed by others.

1. LAMINAR SEPARATION / TURBULENT REATTACHMENT

1.1 Introduction

Laminar boundary layers are prone to the formation of separation bubbles in an Adverse Pressure Gradient (APG). Boundary layer separation occurs in many practical flow configurations. For example, separation bubbles commonly occur on wings at a high angle of attack. Separation bubbles are inherently unsteady and the flow downstream of the reattachment is often turbulent. Most prior investigations of laminar separation have been concerned with mean flow structure. The work reported here is primarily concerned with the unsteady aspects. Much of the material in this section has not been previously published in the archival literature. Therefore the results are presented in some detail.

1.2 Flow Conditions

The layer develops on a 1m (39 inch) wide, flat aluminum plate forming the test-section floor of a small stand-alone open-return wind tunnel. The plate is supported above an optics table, which also serves as an extremely flat and rigid mounting platform for a high-speed computer-controlled 3D probe traverse. A flexible ceiling is contoured to produce the pressure distribution, and two rigid Plexiglas sidewalls complete the test-section. A scaled side view of the test section is shown in Figure 1.

The pressure distribution is essentially the same as that used by Spalart and Watmuff (1993). This pressure distribution was specifically designed to create an APG *turbulent* boundary layer with a high enough Reynolds number to sustain the turbulence and allow accurate experimental measurements, but low enough for DNS. The design incorporates a region of FPG just downstream of the trip-wire which allows the flow to develop without unduly increasing the local Reynolds number. The APG is then applied rapidly. The APG is only moderate (i.e. the turbulent PG parameter $\beta \approx 2$) and the turbulent layer of Spalart and Watmuff remains attached. Removal of the trip-wire, while maintaining the same ceiling shape and inlet unit Reynolds number, leads to a *laminar* boundary layer which separates in the APG and reattaches about 0.2m (7.9 inch) downstream.

The centerline C_p distributions for the laminar and turbulent layers are almost identical except in the vicinity of the reattachment, as shown in Figure 2. The difference between the laminar and turbulent results can be attributed to the relatively large displacement thickness in the vicinity of the separation bubble. Phase-averaged measurements are presented below, in which a small disturbance is introduced at the C_p minimum at x=0.6m (23.6 inch). The C_p measurements for this case are shown separately because the centerline reattachment point moves slightly upstream. The unit Reynolds number based on the inlet reference free-stream velocity U_{ref} is 4.28×10^5 m^{-1} (1.30×10^5 ft^{-1}) and it was maintained constant to within $\pm 0.5\%$ during all measurements. The reference velocity is nominally around 6.5 m/s (21.3 ft/s) and the free-stream unsteadiness at the entry to the test-section is 0.12%.

1.3 Experimental Techniques

1.3.1 Automation of the Experiment

A sophisticated high-speed computer-controlled 3D probe positioning system has been integrated into the test section. The maximum traversing speed in the x-direction is 1.5 m/s (4.9 ft/s) which is sufficient for flying hot-wire measurements in the region of reversed flow. A microVAX 3600 computer is used to control tunnel speed, probe traversal and data acquisition. A high-speed 15-bit Tustin ADC is used for double-buffered data acquisition and processing.

Processing of data in real-time is an important requirement for these experiments due to the total volume of data acquired i.e. storage of raw data for post-experimental processing is impractical owing to the excessively large disk storage requirements. Therefore considerable time was spent optimizing the double-buffered data acquisition/ processing algorithms so that the real-time processing did not introduce significantly longer run-times (see Watmuff 1995a). Briefly, two arrays are set aside in computer memory. Data is acquired and transferred to each array alternately. True double-buffering allows previously acquired data that are stored in one buffer to be processed, while data are simultaneously acquired and transferred to the other buffer. High-speed algorithms for processing the hot-wire data provide a system throughput of 75Ksamples/s for single wires and 25Ksamples/s for cross-wires. These rates can be sustained indefinitely despite the fact that the calculations are performed in double-precision. The same benchmark calculations performed on a 150-MHz Alpha AXP computer indicate that real-time processing rates in excess of 5 Msamples/s are possible, which is high enough for multiple probes in supersonic flow.

A considerable investment in both hardware and software has enabled all the experimental procedures to be totally automated. Redundant safety measures and error detection/recovery schemes are located at each stage throughout the code. Complex 3D measurement grids can be designed and viewed ahead of time. Program execution may be interrupted asynchronously at any stage for any purpose, such as modification of control variables or verification of hardware functions, and then restarted without loss of continuity. At a higher level, hot-wire calibration drift is monitored at regular intervals and new calibrations are performed and the measurements are repeated (automatically) until the drift is within a specified tolerance (typically 0.5%). Operation of the facility has been refined to the point where experiments can be performed continuously (24 hours/day) over several weeks without manual supervision.

1.3.2 Phase-averaged Measurements of Disturbance

Gaster and Grant (1975) studied the evolution of a 3D dispersive TS wave packet by deliberately introducing a small amplitude impulsive disturbance into a Blasius boundary layer. The linear behavior of the wave packet can be predicted by LST (Linear Stability Theory). However, attempts to observe the final nonlinear evolution of the wave packet into a turbulent spot have not been as successful. One explanation for this lack of success is that there is considerable variance in the downstream position for the formation spots. To avoid the spatial jitter of the spot as a whole, most experimental studies of turbulent

spots have used rather large disturbances (e.g. an electric spark or a strong impulsive jet through a hole in the wall) to force the formation of the spot to occur close to the source of the disturbance. These measurements suggest that a spot consists essentially of one or two large eddies. However, flow visualization studies have demonstrated that a typical spot appears to consist of an array of vortex loops. Evidently, there is also considerable variance in the underlying detailed structure from realization to realization, which causes washout of the data. In many of these studies, natural spot formation was not observed when the disturbance was removed, even very far downstream. It is not known whether spots generated in laminar layers which are far from instability, are representative of spots that develop from much smaller disturbances which lead to the formation of wave packets.

Following Gaster and Grant, a small amplitude impulsive disturbance (a "puff") was repetitively introduced through a 0.6mm (0.024 inch) diameter static pressure tapping located at the C_p minimum, as shown schematically in Figure 1. One of the benefits of the APG, used in the present study, is that very small disturbances can be used which lead to downstream transition to turbulence (the reattachment) within a very small range of streamwise positions. Examination of hot-wire signals in the vicinity of the reattachment revealed that complex large-amplitude velocity fluctuations could be generated in a very repetitive manner. The repetitive nature of the complex signals in the reattachment region suggested that phase-averaged data would not suffer from washout owing to phase jitter and that the detailed motions could be measured on spatially dense grids. Further downstream, in the turbulent boundary layer established after the reattachment, the hot-wire signals appeared to be fully turbulent and uncorrelated with the disturbance. However, cursory measurements indicated that phase-averaged data could be extracted far downstream of the reattachment region, although the amplitude was very small.

The size of the perturbation could be made very small without diminishing the relative magnitude of the phase-averaged data. This is an important consideration since the observations are likely to be more representative of the type of instabilities generated by small background disturbances. This is in contrast with the spot studies mentioned above, where the large disturbances could "bypass" known transition mechanisms.

The averages at each point were derived from 25,600 samples, taken at intervals corresponding precisely to the 64 phases used to describe each cycle i.e. a population of 400 disturbance cycles for each phase interval.

1.3.3 Measurement Grids

The location and size of the measurement grids have proved to be a source of confusion during presentation of this material. Details of all the grids are listed in Table 1 for reference.

Normal hot-wires can be positioned very close to the wall and this makes them superior to crossed-wires for measuring the thin laminar velocity profiles i.e. δ=6 to 10mm (0.24 to 0.39 inches). Also, the effects of high shear are almost negligible and they are less susceptible to error in regions of high turbulence intensity. Normal hot-wire data are also useful for testing the scaling of the downstream turbulent boundary layer. Broadband normal hot-wire profiles have been measured along the centerline of the entire test section.

x (m) Start	x (m) End	δx (mm)	N_x	N_y	N_z	Flow Regime
Broadband Normal Hot-Wire, Centerline Planes						
0.10	0.55	50	10	25	1	Development in FPG
0.56	0.70	20	8	26	1	FPG through separation in APG
0.72	0.90	20	10	37	1	Separated APG through Reattachment
0.95	2.00	50	22	37	1	Turbulent
Phase-Averaged Normal Hot-Wire, Spanwise Planes						
0.59	0.78	10	21	17	11	Linear behavior of disturbance
0.79	0.90	10	12	17	25	Nonlinear formation of roll-ups
0.91	1.00	10	10	17	41	Formation of Vortex Loops
Broadband & Phase-Avged Cross-Wire, Centerline Planes, *UV* orientation of probe only						
0.750	0.897	3	50	17	1	Linear Disturbance through Reattach
0.900	1.096	4	50	17	1	Formation of Vortex Loops
1.100	1.345	5	50	17	1	Turbulent
1.350	1.644	6	50	17	1	Turbulent
1.650	1.993	7	50	17	1	Turbulent
Broadband & Phase-Avged Cross-Wire, Spanwise Planes, *UV* & *UW* orientations of probe						
x (m) Start	z (mm) ± max	δz (mm)	N_x	N_y	N_z	Flow Regime
0.801	60	3	-	17	41	Linear Dispersive Wave Packet
0.825	80	4	-	17	41	Nonlinear Dispersive Wave Packet
0.849	100	5	-	17	41	Just prior to Reattachment
0.900	200	10	-	17	41	Turbulent
1.000	200	10	-	17	41	Turbulent
1.250	200	10	-	17	41	Turbulent
1.500	200	10	-	17	41	Turbulent
2.000	200	10	-	17	41	Turbulent
Phase-Avged Cross-Wire, Full 3D Grid, *UV* & *UW* orientations of probe						
x (m) Start	x (m) End	δx (mm)	N_x	N_y	N_z	Flow Regime
0.75	1.080	7.5	45	17	41	Linear Wave Packet through Vortex Loops

Table 1. Measurement grid details for Laminar Separation/Turbulent Reattachment study.

Phase-averaged normal hot-wire data have been measured on 42 spanwise planes, at 10mm intervals along the test-section.

Cross-wires provide both the streamwise and one of the cross-stream velocity components. Phase-averaged cross-wire data were measured on a centerline streamwise plane normal to the wall, containing (N_x, N_y)=(250, 17) data points. The origin for these grids is in the separated laminar layer where the wave packet is still showing linear behavior. Only the *UV*-orientation of the probe was used for this centerline plane. In an effort to capture the three-dimensionality of the flow, data were measured on eight spanwise planes, normal to the test surface. The data for the spanwise planes contain *U*, *V* and *W* data requiring that the measurements be performed twice (once for the *UV*- and again for the *UW*- orientations of the cross-wire probe). Temporal mean velocity and broadband Reynolds stress measurements have also been measured without the disturbance. The same streamwise and horizontal grids were used while only five of the spanwise planes normal to the wall were used for the comparison.

The formation of vortex loops in the reattachment region was measured in detail using a true 3D grid of dimension (N_x, N_y, N_z)=(45, 17, 41). The 31,365 grid points were also measured twice, using both orientations of the crossed-wire probe, to obtain all three velocity components. These measurements required 31 days of continuous operation of the automated facility.

1.4 Results

1.4.1 Mean Flow

The flow can be divided into four distinct regions as labeled in Figure 1. The first region, labeled (1), is where the laminar boundary layer develops in the FPG. The layer separates in the APG in region (2), leading to the formation of a detached shear layer. Region (3) is characterized by rapid growth of unsteadiness and the turbulent reattachment. Region (4) consists of the turbulent boundary layer downstream of the reattachment.

Laminar Layer in the FPG

The test plate forms an extension to the lower surface of the contraction. This is an undesirable configuration for laminar flow studies, since the origin and upstream history of the boundary layer at the entrance of the test section are unknown. However the FPG provides several beneficial effects i.e. it presents a stabilizing influence, which improves the spanwise uniformity of the layer, and it is responsible for the development of a self-similar profile shape.

A region of approximately 20 boundary layer thicknesses in length exists in the FPG region where the free-stream velocity follows a power law i.e. $U_\infty \propto x^m$. The value of m=0.28 was derived numerically from a cubic spline applied to the C_p distribution, assuming that the free-stream and wall static pressures are equal at a given x. In an attempt to characterize the layer in this region, the profiles were fitted to the Falkner &

Skan similarity solution using the wedge angle determined from the curve fit applied to the C_p distribution i.e. $\beta = 2m/(m+1) \approx 0.44$. The only adjustable constant was the effective origin, which was calculated using a least squares technique. Three experimental profiles are shown in Figure 3(a) using the same optimum effective origin of -0.56m (-1.84 ft) along with the Falkner & Skan solution. The shape factors, H=2.34, 2.31 and 2.34 corresponding to profiles at x=0.45m, 0.50m and 0.55m (1.48 ft, 1.64 ft and 1.80 ft) are in reasonable agreement with the Falkner & Skan value of H=2.39 for β=0.44. The reasonably good fit of the experimental data suggests that the Falkner & Skan similarity solution would form a suitable inlet boundary condition for a numerical study of the separation in the APG.

The momentum thicknesses for the three profiles in Figure 3(a) are 0.668mm, 0.651mm and 0.654mm (0.0263, 0.0256, 0.0257 inches) respectively. The Reynolds numbers based on the momentum thickness and the local free stream velocity are θ=317, 318 and 331 respectively.

Laminar Layer in the APG

The free-stream velocity variation with streamwise distance in the APG region (2) also follows a power law for a short distance where β= - 0.74. This is much larger than the Falkner & Skan value for separation i.e. β= -0.2. Flying hot-wire measurements (described later) have been used to estimate the streamwise location of the separation point at x=0.64m (2.10ft) and reattachment point x=0.86m (2.82ft) on the centerline. Mean velocity profiles obtained with a stationary normal hot wire in the APG are plotted in three groups in Figures 3(b), (c) and (d). The profiles in Figure 3(b) that are downstream of the separation clearly show the start of the progression of the detached shear layer away from the wall. The reverse flow that occurs close to the wall cannot be determined with a stationary probe owing to hot-wire directional ambiguity. Further, rectification of the hot-wire signals will occur, if the magnitude of the unsteadiness causes the velocity to change sign. The positive error owing to rectification will be largest when the mean flow is zero, which is one explanation for why the profiles do not contain points of zero velocity. The profiles for x=0.7m (2.30 ft) to x=0.8m (2.62 ft) are shown in Figure 3(c). The continued progression of the detached shear layer away from the wall is apparent. The effects of hot-wire rectification, mentioned above, are also clearly visible. However the broadband unsteadiness remains quite small in this region and the errors in the region of reversed flow remain fairly small.

Reattachment Region

The broadband unsteadiness increases very rapidly for x > 0.8m (2.62 ft) and the effects of hot-wire rectification become very pronounced near the wall, as shown in Figure 3(d), especially in the vicinity of the mean reattachment. Reynolds stress contours in a plane parallel to the test surface (not shown) and naphthalene flow visualization tests indicate that the mean reattachment is very two-dimensional. Furthermore, the naphthalene flow visualization estimate of the location of the reattachment line agrees very well with the location on the centerline determined by the flying hot-wire measurements described below.

Flying Hot-wire Investigation of the Separation Bubble

The flying hot-wire technique involves propelling the probe in the upstream direction while measurements are made on the basis of the probe position. The upstream velocity of the probe traverse must be measured as well so that the velocity relative to a stationary observer can be obtained by subtraction. Each upstream passage of the probe traverse results in a single sample at each position. Ensemble averages for the mean flow and Reynolds stresses are obtained by repeating the motion a sufficient number of times for statistical convergence of the data. Although it can be relatively time consuming to perform a large number of upstream traverse passes, one advantage of the technique is that the measurements can be obtained for a large number of closely spaced data points in parallel. Another advantage is that the superimposed bias velocity reduces the magnitude of the velocity fluctuations relative to the increased velocity seen by the probe. Accurate measurements are possible in regions of reversed flow. The maximum speed of the probe traverse in the x-direction is 1.5 m/s (4.9 ft/s) and this proved to be sufficient to overcome the small magnitude of the reversed flow in the separated region.

Unfortunately, the total time for a single measurement cycle is quite long i.e. around 8 seconds. However, the primary objective for performing the flying hot-wire measurements was to measure the reverse flow within the separated region. Since the flow in the separated region is relatively steady, only 500 upstream passes were required for adequate convergence of the mean flow. The mean velocity relative to a stationary observer, U, and the mean square of the fluctuating component, u^2, measured with a single hot-wire are shown in Figures 4(a) and (b). Data were obtained at wall distances as close as y=0.5mm. While a greater number of samples would be required for convergence of the mean square of the velocity fluctuations, the convergence of U is sufficient to determine the streamwise location of the point, U=0, at each y-position, with some certainty.

The region of reversed flow is confined within a wall distance of about 4mm. Unfortunately this region is very thin and a direct examination of the mean velocity vectors using crossed-wires has not been performed. However, it is possible to deduce a plausible representation of the temporal mean separation bubble from the normal hot-wire data. The two points of zero velocity for y < 4mm are plotted in the x-y plane in Figure 5. These points are joined by dashed lines, which are extrapolated to the wall to provide an estimate of the streamwise location of the separation point i.e. $x \approx 0.64$m (2.1ft), and the reattachment point i.e. $x \approx 0.86$m (2.82ft). The region between the two lines contains reversed flow and the tangent to the streamlines that cross each line must be in the y-direction (since $dy/dx=\infty$ for U=0). This information acted as a guide for sketching the mean flow streamlines as seen by a stationary observer.

Comparisons of the inner region of stationary and flying hot-wire mean velocity profiles approaching reattachment are shown in Figure 6. Although the size of the region of temporal mean reverse flow diminishes approaching reattachment, the relative extent of the region effected by rectification errors increases, because of the larger amplitude fluctuations that are experienced approaching the reattachment.

The scaling for the mean flow has not been extensively explored at this stage. However it is noted that Curle & Skan (1957) proposed a separation criteria based on the parameter,

$$S = (\theta^2_{sep}/\nu)\ (\partial U/\partial x)_{sep}$$

At the centerline separation point, $(1/\nu)(\partial U/\partial x)_{sep}$= -0.16x10^{6}m^{-2} and θ_{sep}=0.76mm (0.030 inch) giving a value of S = -0.092. Curle & Skan found -0.171 < S < -0.068 for the onset of separation. Therefore the value observed in this experiment is consistent with the Curle & Skan criterion for the onset of separation.

Downstream Turbulent Boundary Layer

Extensive measurements have also been made in the turbulent boundary layer downstream of the reattachment. The results will not be discussed in detail here. Briefly, the properties of the layer are markedly different to the flow of Spalart and Watmuff (1993), despite using the same unit Reynolds number and pressure distribution. The most notable differences are that the skin friction is almost double, and the Reynolds stress profiles have peaks close to the wall, rather than in the central region of the layer.

1.4.2 Phase-averaged Measurements

As mentioned previously, a small-amplitude impulsive disturbance was repetitively introduced through a small hole in the test surface as shown schematically in Figure 1. The evolution of the disturbance has been tracked from its source, all the way into the reattachment region and beyond into the fully turbulent boundary layer.

Formation and Development of Dispersive Wave Packet

Stationary phase-averaged (64 phase interval) normal hot-wire data have been measured on 42 spanwise *yz*-planes at 10mm (0.39 inches) intervals along the test section, from just upstream of the hole, to about 0.2m (7.9 inches) downstream of the reattachment. Directly above the hole, the disturbance penetrates only 1mm into the layer ($\delta \approx 6mm \approx 0.24inch$) and it leads to a maximum negative amplitude of $0.03U_{ref}$. The maximum rms amplitude of all the phase-averaged waveforms for all points in each spanwise plane, is plotted against streamwise distance in Figure 7. At first, the layer is attached and the rms amplitude decays exponentially. The rate of decay slows after the separation and reaches a minimum, before undergoing exponential growth for 0.72m> x > 0.80m (2.36 ft > x > 2.62 ft). The exponential growth rate implies that the wave packet behavior is linear, despite reaching a rather large amplitude of $(u_\phi)_{rms\ max}/U_{ref} \approx 20\%$.

Selected phase-averaged waveforms are shown in Figure 8. The small oscillations superimposed on the overshoot following the main large negative perturbation in Figure 8(a), could be the result of transient oscillations in the shaker-diaphragm-tube system used to inject the disturbance (see Figure 1). The waveforms at the temporal mean separation point in Figure 8(b) have much the same shape. However, at the point of minimum amplitude in Figure 8(c), an almost equal magnitude positive wave has emerged ahead of the original negative perturbation.

$\delta_\omega = \Delta U/(\partial u/\partial y)_{max}$ and the velocity ratio $\lambda = (\Delta U)/(2U_m)$ may be used to characterize the layer. Following Monkewitz & Huerre (1982) and Michalke (1964), the most amplified frequency may be expressed nondimensionally as $\omega^* = \frac{1}{4}\, \delta_\omega\, (2\pi f)/U_m$. The most amplified frequency predicted from inviscid linear stability theory for a parallel shear flow with a tanh profile is $\omega^* = 0.21$.

The low Reynolds number of this investigation implies that the effects of viscosity may be important. Further, the mean flow is nonparallel owing to the presence of the APG. However, the nondimensional frequency ω^* predicted from LST is not strongly dependent on either λ or the profile shape. Therefore this parameter may provide further evidence that the instability mechanism is inviscid. The following method was used to calculate ω^*. In contrast with a free shear layer in a ZPG, the free-stream velocity at the edge of the separated layer is ill-defined i.e. $U(y)$ does not tend to a constant as $y \rightarrow \infty$. The uncertainty is most pronounced in the vicinity of the reattachment. The maximum velocity was used for U_1. The flying hot-wire data was used to estimate U_2. The velocity gradient $(\partial u/\partial y)_{max}$ was estimated numerically after visually identifying the region of linear variation in the profiles shown in Figure 3. The frequency f was obtained from the well-defined spike in the corresponding power spectra measurements (obtained without the disturbance). The frequency f closely corresponds to the disturbance frequency estimated from the wavelength and propagation velocity of the wave packet. An approximately linear variation of ω^* with streamwise distance was obtained in the region of exponential growth i.e. $\omega^* \approx 0.10$ at x=0.70m increasing to $\omega^* \approx 0.25$ at x=0.84m. The LST value of $\omega^* = 0.21$ corresponds to $x \approx 0.80$m which is where the large-scale roll-ups are observed to form in the phase-averaged measurements (see Figure 12). This observation provides further evidence that the instabilities are inviscid rather than of viscous origin.

Formation of Vortex Loops in the Reattachment Region

An animation sequence of the spanwise vorticity contours derived from cross-wire data in a centerline plane is shown in Figure 13. The streamwise distance between the grid points is 3mm (0.12 inches) and 17 uniformly spaced grid points are used normal to the wall. The formation of the roll-ups in the initial stages is reminiscent of a free shear layer. Four distinct regions of concentrated spanwise vorticity emerge from the detached shear layer which are labeled A, B, C and D. The first region, labeled (A), appears to be short-lived while the second region of concentrated spanwise vorticity (B) accelerates away from the wall to become the dominant member of the group.

The regions of concentrated spanwise vorticity in Figure 13 correspond to sections through three-dimensional vortex loops. This region has been mapped in detail using a true 3D grid of dimension $(N_x, N_y, N_z) = (45, 17, 41)$. The 31,365 grid points were measured twice, using both orientations of the crossed-wire probe, to obtain all three velocity components. An animation sequence of surfaces of constant vorticity magnitude calculated from the data is shown in Figure 14. The data has not been interpolated and no smoothing has been applied. The evolution of the 3D waves into a group of large-scale vortex loops is clearly visible. At first, the loops are only slightly bowed and the vorticity is mostly aligned in the spanwise direction. With subsequent development, the "legs" move together while the tops rapidly accelerate away from the wall leading to the formation of

the elongated vortex loops. Compromises must be made in selecting the viewing parameters and the single representative contour surface level for the animation sequence. The smaller loops located off the centerline are difficult to ascertain. Some of the smaller off-centerline loops can be seen in Figure 14, for $z < 0$ at Phase 55. In a plane parallel to the wall (not shown) the contours of phase-averaged vorticity magnitude appear to be confined to wedge-shaped region that is reminiscent of a turbulent spot. However it should be emphasized that the surrounding flow is highly unsteady.

Reynolds stress measurements are less susceptible to errors originating from hot-wire calibration drift and other spurious errors, compared to the velocity measurements which must then be differentiated to calculate the vorticity. The Reynolds stress can be resolved into a Contribution resulting from the perturbations of the phase-averaged velocities and a Background component resulting from the random motion at constant phase. Both are phase-averaged quantities and the total Reynolds stress is given by sum of each quantity, averaged over all phases. A formal definition of these quantities is given by Watmuff (1991b). The Background component originates from two sources i.e. fluctuations due to small-scale random motions superimposed on the large-scale motions and dispersion, introduced by phase jitter and the physical differences between successive structures. Unfortunately, it is not possible to differentiate between the effects of fine-scale motions and dispersion. Furthermore, it is difficult to determine whether the dispersion originates from essentially the same vortex loop appearing at slightly different positions upon each realization (phase jitter) or whether there are small local differences between successive vortex loops.

Color contours of the Contribution and Background Reynolds stresses are shown on the centerline plane in Figure 15 for Phase 47. The corresponding spanwise vorticity contours are superimposed as solid black lines. At this stage of development, the Contribution of the phase-averaged velocity components to the Reynolds stress is larger than the random Background components.

The Contribution to the Reynolds stress can be explained by modeling the vortex loops (and their images in the wall) with a number of straight line segments containing an radial exponential vorticity distribution and using the Biot-Savart law for calculation of the induced velocities. The Biot-Savart calculations indicate that the largest streamwise component of the induced velocities is in the upstream direction and occurs between the "legs" of the vortex loops. The calculations are consistent with the contours shown in Figure 15(d). The larger level associated with loop B (see Figure 13) is the result of the larger curvature, compared to loop A which is more two-dimensional. The Contribution to the Reynolds stress in the direction normal to the wall are shown in Figure 15(f). These contours are also consistent with Biot-Savart calculations. However the distribution is asymmetrical since there is some cancellation of the induced velocity between the loops. The Contribution to the Reynolds shear stress in Figure 15(e) can be divided into four quadrants based on the sign of induced velocities. The quadrants are spatially related to the distribution of the contours. However the induced velocities from the legs of the loops lead to the 2nd and 3rd quadrants (closest to the wall) being dominant.

The spatial distributions of the random Background Reynolds stress contours in Figures 15(a), (b) and (c) are more uniform than the periodic Contribution components. Large levels of the streamwise component are observed to extend from regions of concentrated vorticity down towards the wall while the component normal to the wall is more locally concentrated. The Background component of the shear stress is almost entirely negative except for a small region of low positive magnitude which can be found in the vicinity of x=0.9m. It is tempting to attribute the Background Reynolds distribution to the development of fine-scale motions associated with the vortex-loops. However, as stated previously, it is impossible to differentiate between the effects of dispersion and the presence of fine-scale motions.

Vortex Loops in the Downstream Turbulent Boundary Layer

Phase-averaged cross-wire data (*UV*-orientation only) have been measured in a number of sequential centerline planes in the turbulent boundary layer downstream of the reattachment. The results from each grid have been combined to form a composite data set on a single grid. Cross-wire data (using both probe orientations) have also been measured in a number of spanwise planes (see Table 1). The increased phase jitter and the presence of fine-scale turbulent motions cause the magnitude of the phase-averaged velocity perturbations to be much smaller in the downstream turbulent boundary layer e.g. the maximum rms of the phase-averaged streamwise fluctuations at x=2.0m is an order of magnitude less than the peak value observed in the reattachment region.

It is well known that the flow pattern generated by a velocity vector field depends on the velocity of the observer. The presence of the temporal mean velocity gradient at the wall makes it difficult to select an observer velocity such that the effect of the relatively large temporal mean velocity is reduced. Furthermore, the small magnitude of the phase-averaged perturbations adds to the difficulties of interpretation of the *total* phase-averaged velocity vector flow field since the temporal mean velocity components are considerably larger. Small measurement errors in the temporal mean flow quantities introduce considerable scatter since the errors are of comparable size to the phase-averaged perturbations. Therefore representative phase-averaged velocity *perturbation* vectors are shown in Figure 16(a). The flow pattern generated by the velocity perturbation vector field avoids many of the difficulties mentioned above but it is difficult to attach precise meaning to the flow pattern.

Vorticity is a quantity that is independent of the velocity of the observer. The corresponding contours of the phase-averaged spanwise vorticity *perturbations* are shown in Figure 16(b). The overall shape of the spanwise vorticity perturbation contours changes very little for different streamwise positions. However, the reduced magnitude of the phase-averaged perturbations and small measurement errors in the temporal mean velocity components, have the combined effect of introducing considerable scatter into the *total* phase-averaged vorticity contours. The scatter increases with increasing streamwise distance. Corresponding total phase-averaged vorticity contours are shown in figure 16(c). The effects are not severe at this streamwise position, but by x=2.0m, the total vorticity contours show considerable scatter, while the perturbation contours have much the same appearance as those further upstream.

The small rate of change of the vorticity perturbation contours with streamwise distance suggests that Taylor's hypothesis can be applied to the spanwise grids to generate representative fully 3D data sets. Figure 16(d) shows the total phase-averaged vorticity contours obtained by applying Taylor's hypothesis for phase to the centerline data on the spanwise plane located at x=1.5m. A uniform scaling was used for transforming ϕ to x which was determined from a local linear fit to the phase of the peak values of u_ϕ as a function of x. The reasonably good agreement between the contours in Figures 16(c) and (d) suggests that the 3D data generated from the spanwise planes provides a close approximation to the true spatial 3D information (which has not been measured).

Complete (u,v,w) 3D velocity vector fields have been generated using Taylor's hypothesis applied to the spanwise planes located at x=1.0m, 1.25m, 1.5m and 2.0m. Contour surfaces of the corresponding total and perturbation vorticity magnitude are shown in figures 17(a) to (h). Each figure also contains color contours on the centerline plane and on a plane parallel to the wall. The wall distance of the plane parallel to the wall was chosen to aid interpretation of the 3D data.

The perturbation (Figure 17a) and total (Figure 17b) vorticity magnitude distribution at x=1.0m provide additional feedback on the accuracy of Taylor's hypothesis for generating 3D flow fields from the spanwise planar measurements. The greatest deviation from the true spatial distribution is expected to occur at this position because the streamwise derivatives of flow quantities are still quite large. The flow field generated from this spanwise plane overlaps the true spatial measurements in Figures 13 and 14 (e.g. Phase 55) and a comparison reveals that the salient features have been reproduced i.e. there are three vortex loops.

Further downstream at x=1.25m, the contours of vorticity magnitude in Figures 17(c) and (d) clearly show the presence of a vortex loop which has been traced back to the dominant loop which emerges in the upstream reattachment region. This loop is labeled B in Figure (13). Both the perturbation and total vorticity contour surfaces indicate that the vorticity is more concentrated in the outer region of the loop. The "legs" of the loop extend down close to the wall but this is not indicated for the chosen contour surface level. There are two additional noteworthy regions of concentrated vorticity present in the total vorticity magnitude distribution in Figure 17(d). The first region is located near the wall in the vicinity of the centerline between the legs of the loop. It should be emphasized that this region is distinctly separate from the legs of the loop. The local "upwelling" of the concentrated vorticity at the wall can be explained in terms of the induced velocities generated by the loop. The second noteworthy region consists of a pair of upwellings of near wall vorticity symmetrically displaced from the centerline downstream of the loop. It is difficult to explain these upwellings in terms of velocities induced by the vortex loop. These regions may be related to remnants of the first distinct roll-up labeled (A) in the reattachment region.

The loop and the two regions of concentrated vorticity can also be seen in the total vorticity contours at x=1.5m in Figure 17(f). The local upwelling of near wall vorticity between the legs can be more clearly seen in the centerline plane of the true spatial contours of Figure 16(c) in the vicinity of x=1.4m. As mentioned previously, the phase-

averaged velocity perturbations are considerably weaker at x=2.0m and the large scatter is apparent in the total vorticity contours shown in Figure 17(h). However the loop is still clearly visible in the perturbation contour surface shown in Figure 17(g).

1.5 Concluding Remarks

The "passing frequency" of the phase-averaged disturbance calculated from the wavelength and phase velocity corresponds closely to the frequency of the spike observed in the power spectra when the disturbance is not present. This implies that the phase-averaged observations are representative of the naturally occurring instabilities in the flow. The decay of the disturbance while the flow is attached suggests that the layer is viscously stable. There is good evidence that the growth that occurs after separation is due to an inviscid Rayleigh type of instability in the detached shear layer. The nondimensional roll-up frequency is closely the same as that predicted by LST for a parallel shear layer in a ZPG. The growth of the instabilities and the subsequent roll-up and formation of vortex loops ultimately leads to the turbulent reattachment.

The dominant phase-averaged vortex-loop formed in the reattachment region retains its identity some 20 layer thicknesses downstream in the fully turbulent boundary layer. The phase-averaged velocity field and Reynolds stress distribution surrounding the vortex loop are of some interest since many workers have proposed that vortex loops are the dominant coherent structure underlying turbulent boundary layers in general.

The flow will provide a challenging test case for CFD yet the Falkner & Skan velocity profile in the FPG provides a simple and convenient inlet boundary condition. The differences between the turbulent boundary layers (i.e. Spalart and Watmuff) in the downstream region are interesting because the same unit Reynolds number and pressure distribution were used. Both flows will provide a significant challenge for advanced code development and for testing turbulence models. A more complete description of this work will be submitted for publication in an archival journal.

2. DISTURBANCES GENERATED BY SUCTION HOLES FOR LAMINAR FLOW CONTROL

2.1 Introduction

The beneficial effects of suction for delaying transition to turbulence have been known for some time but it is only recently that the technology has become available to produce large sheets of perforated material for use in aircraft wings at reasonable cost. Flight tests have been conducted recently using porous surfaces containing around 10^9, 0.002 inch diameter laser drilled holes. The drag reduction obtained by maintaining laminar flow over a substantial portion of the wing surface potentially offers considerable fuel savings. Suction, as a means for Laminar Flow Control is being seriously considered for production aircraft in the near future.

Many engineering design tools for predicting the transition location assume that the suction is uniform. In some cases there is evidence to suggest that the discrepancy between the predicted and observed transition location may be due to local 3D disturbances that are generated by the discrete holes. It is known that a pair of streamwise vortices are generated by a hole when the suction is strong. Designers of porous surfaces use Goldsmith's Criterion to minimize *cross-stream* interaction between these vortices. However nothing is known about the *streamwise* interactions that are likely to be even more important. The objective of this project is to determine the characteristics of disturbances generated by suction holes, and whether they decay or amplify with streamwise distance, and the nature of the interactions between disturbances generated by different holes, which are aligned, but displaced in the streamwise direction.

2.2 Modifications to the Wind Tunnel

A 2D elliptic leading edge of 24:1 aspect ratio was built to establish a new laminar boundary layer on the test surface which is located on top of a baffled plenum chamber box. The surface of the leading edge has been hard anodized and hand polished. The leading edge is located in the free stream, 0.2m (7.8 inches) downstream of the contraction exit to avoid adverse pressure gradient effects. It is common practice to mount laminar flow test surfaces on legs within the test section and to adjust the stagnation point using a flap attached at the rear. The depth of the plenum chamber box below the suction surfaces excluded this type of installation so the following alternative was used. Curved sheet metal is attached to the underneath of the leading edge. The sheet metal acts in conjunction with an extension to the contraction exit to form a curved slot for redirecting the excess test section flow (i.e. below the leading edge) out into the laboratory. The relationship between these components can be seen in Figure 19.

The presence of the 3D probe traverse causes the test section pressure upstream of it to be slightly higher than the ambient pressure in the laboratory. The leading edge stagnation point is set by adjusting the width of the slot which passively controls the flow

rate of excess air into the laboratory. Rms velocity fluctuations (u_{rms}) measured with a hot-wire located within the layer at x=1.0m (3.28 ft) were used as a guide for setting the stagnation point. High levels of unsteadiness are observed when the stagnation point is located below the leading edge (owing to flow separation) while the effects are much less when the stagnation point is located above the leading edge. A plot of u_{rms} versus slot width was used to set the stagnation point. The final slot width was selected to correspond to the u_{rms} minimum based on the assumption that this setting corresponds with stagnation point flow.

Typical porous surfaces for LFC consist of 0.002 inch diameter holes on a 0.020 inch square grid. This hole size and spacing is too small to resolve flow disturbances. Consequently, this hole size and grid spacing has been scaled up by a factor of 20 to provide greater spatial resolution for the hot-wire measurements. Figure 18 shows the sizes of the grid and holes relative to the hot-wire probe. The test surface consists of 8466 holes, 0.040 inch diameter, spaced on a 0.400 inch grid, which were individually drilled with precision using an NC machine. Details are given in Watmuff (1994b). This 20:1 scaling provides sufficient spatial resolution to follow the evolution of disturbances downstream of the holes while still maintaining a suction geometry length-scale to boundary thickness ratio that is representative of flight conditions. The porous surface was designed to be as wide as possible to minimize contamination from the boundary layers forming over the solid edges. Another impervious test surface was constructed for establishing the Blasius base flow and for the isolated hole studies. This test surface is identical in all respects to the porous surface described above (with the exception of the suction holes).

A baffled plenum chamber box is used to gather the flow through the porous surfaces into tubes which are routed to a high pressure fan which acts as the suction source. Longitudinal- and cross- sections through the test section showing the suction system are shown in Figure 19. A critical design objective was to achieve high uniformity of the suction flow rate. The pressure differential across the suction surface in the streamwise direction is affected by the pressure drop across the probe traverse. The plenum chamber box is divided into 17 baffles in the streamwise direction to isolate the upstream suction from the presence of the traverse. Another benefit of dividing the box into a number baffles is that the "contraction ratio" is reduced for the flow into the tubes connected to the suction source. As a further means of reducing this contraction ratio, each baffle is subdivided using two custom built inverted bathtub shaped ABS plastic "contraction cones". The smooth curves of the plastic should also help achieve a steady flow within the baffle. The flow is gathered from each baffle into two rigid 1 inch diameter schedule 80 PVC tubes which are joined via a tee below the baffle box. The flow from each baffle then continues within a single tube.

The 17 tubes routed beneath the plenum chamber box are terminated at a convenient outlet point below the test section. Flexible tubes connect the outlets to 5 micron air filters which are located upstream of a bank of flow meters. The filters act as sound and vibration dampers in addition to ensuring that the flow meters are kept clean of contaminants. The flow meters act as convenient visual monitors and are not used for accurate suction flow rate measurements. Each baffle is fitted with a static pressure tap so

that the suction flow rate can be individually calibrated against the pressure differential using the same instrumentation. The static pressure inside the baffle is used to determine the flow rate under run conditions. Flexible tubes join each flow meter to a common 9 inch diameter manifold which is connected to the high pressure blower that acts as the suction source. The blower can provide a maximum of 45 inches of water suction pressure which corresponds to individual baffle flow rates of 10 cfm. For a free stream velocity of 20 m/s this corresponds to a Suction Coefficient C_q=20 x 10^{-4} which is an order of magnitude greater than typical suction requirements. Therefore flow phenomena generated by over suction can be studied. The high pressure centrifugal fan does not exhibit undesirable characteristics such as stall or surge at any speed. The fan is driven by a computer controlled dc motor so that the overall suction flow rate can be controlled automatically by simply adjusting the fan speed.

For the isolated suction hole studies the suction source consists of a miniature venturi which is driven by a PID controlled pressure regulator connected to the general purpose compressed air supply of the laboratory. The volume flow rate is calibrated using a high accuracy flow meter while the output of a differential pressure transducer is measured to provide the corresponding set point voltages. During an experimental run, various suction flow rates can be applied using the output of a computer controlled digital-to-analog converter as the PID set point. The suction pressure is then automatically held constant by the PID regulator by dynamically adjusting the pressure applied to the venturi such that the output of the pressure transducer is equal to the set point.

The addition of the leading edge and slot lengthened the test section and a new full length Plexiglas ceiling was manufactured. Turnbuckles are used to adjust the height of the ceiling to set the ZPG. Spacer blocks were used to raise the traverse assembly and the side walls to correctly position them relative to the new height of the test surface above the optics table which forms the base of the test section. Short extensions were made for the sidewalls to complete the test section. The extensions also act as convenient windows which provide access to the traverse for mounting probes.

2.3 Experimental Techniques

Standard Dantec boundary layer hot-wire probes were modified for these experiments. The overall size of the probes was reduced and the prongs were stiffened by bonding a small cross brace with epoxy. The standard 1mm long, 5μm diameter wires were replaced with 0.5mm long, 2.5μm diameter wires.

Considerable time was spent developing a technique using multiple probes. The potential benefit of using multiple probes is that a significant reduction in the total experimental run time can be realized e.g. measurements requiring a 28 day continuous run with a single probe would take only 4 days if 7 probes were used. The benefit can only be realized if the real-time processing does not act as a bottleneck. To minimize this problem the high level run-time data processing code was further optimized by "in-lining" all computationally intensive loops by hand.

A multiple probe holder was constructed which accepts the standard Dantec probe supports to form a rake of wires with uniform spanwise spacing of 5mm, 10mm or 20mm (0.20, 0.39 and 0.79 inches). Two set screws are used to make small angular adjustments to the probe support axis for alignment. The technique allows the relative height of each probe to be made collinear within 0.02mm (0.001 inches). Final alignment of the probes with respect to the test surface can then be made by aligning the rake as a whole. The advantage of using standard Dantec supports is that individual probes can be replaced without having to remove the entire rake from the test section. However, during initial measurements it was discovered that this arrangement created a local adverse pressure gradient which caused separation of the boundary layer. Wall pressure coefficient measurements were used as a guide for testing mock ups of alternative configurations. The arrangement that produced the least disturbance consisted of thin-walled stainless steel hypodermic tubing projected 152mm (6 inches) upstream from the probe holder and spaced 20mm (0.79inch) apart in the spanwise direction.

The physical layout of the rake restricts the multiple probe measurement grids to being rectangular in the *x-z* plane. The grid spacing must also be uniform in the spanwise direction. However the spanwise grid spacing can be made smaller than the probe spacing. In this situation the traverse has to perform sequences consisting of a number of small moves equal to the grid spacing, followed by a large move to the position of the first probe at the next grid position. Many other software issues occurred with the implementation of multiple probes but these will not be described here.

The application of a small sinusoidal sound disturbance through a pressure tapping has been used to generate 3D Tolmien-Schlichting (TS) waves. A special circuit was built to generate a primary sinusoid in precise synchronization with sampling pulses which are produced at equally spaced phase intervals over the period of the sinusoid. The sinusoidal waveform is stored in EPROM memory and the output is used to drive a 12-bit digital-to-analog converter. The number of phase intervals can be selected from 16 to 256 in powers of two. As the name suggests, the sampling pulses are used to initiate the ADC samples of the hot-wire signals within the boundary layer. The precision offered by the digital circuit removes the phase jitter introduced by instrumentation and allows faster sorting algorithms to be used for data processing. A second sinusoid can be generated with a phase-difference that can be set very accurately, either manually or by digital computer. The purpose of the second waveform is to generate another set of TS waves at a hole downstream of the first hole. The interaction between the two sets of TS waves can be explored as a function of the phase difference. The amplitude and offset of both sinusoids can be adjusted before the signals are amplified to drive the speakers which produce the disturbances.

2.4 Results

2.4.1 Mean Flow and Broadband Unsteadiness

Transformation of the facility for the suction hole studies has been accomplished with some success. The free-stream unsteadiness u/U_∞= 0.08% for a unit Reynolds number Re_x=1.25 x 10^6 m^{-1} (i.e. a nominal free-stream velocity, U_∞=18.5 m/s). Intermittent

bursting is observed at x=1.8m i.e. Re_x=2.25 x 10^6, which is very acceptable for an open return wind tunnel. The skin friction coefficient C_f estimated from the velocity gradient at the wall follows the Blasius distribution within the experimental uncertainty as shown in Figure 20(a). The layer thickness varies from 2.5mm (0.1 inch) to 4.8mm (0.2 inch) over the measurement range and the development also compares favorably with Blasius variation as shown in Figure 20(b). The mean velocity profiles are shown in Blasius coordinates in Figure 20(c) . The experimental shape factors, H, for these 16 centerline profiles range from 2.54 to 2.75 compared to the Blasius value of 2.59.

The profiles of the rms velocity distribution shown in Figure 20(d) have peak values which vary with $x^{1/2}$, which is an indication of the presence of Klebanoff modes. Presently there is no rational scientific explanation for Klebanoff modes but they occur in most facilities. At the time the data was obtained it was thought that they played a passive role because their frequency is so low. However recent measurements by Kendall of JPL indicate that Klebanoff modes tend to inhibit the growth rate and spanwise propagation of 3D TS waves. At this stage it is not known what influence the Klebanoff modes in this facility have exerted on the TS waves.

2.4.2 Single Isolated Hole Studies

Single isolated hole studies were performed using the pressure tap holes on the centerline of the impervious plate which was used to verify the acceptability of the Blasius base flow. Experiments concerning suction hole disturbances have consisted of the introduction of a harmonic disturbance at an isolated hole via a speaker attached to a pressure tap line. The streamwise location of the hole corresponds to Re_x=1 x 10^6, and the nondimensional frequency $F=2\pi\nu/U_\infty^2$=40 x 10^{-6} closely corresponds to most amplified mode at this Reynolds number.

Initial (64 interval) phase-averaged measurements were performed without suction using a 2D centerline planar grid consisting of 161 streamwise profiles originating just upstream of the hole at x=0.855m and ending at x=1.6m (i.e. 5mm intervals). Each profile consisted of 30 y-positions spaced uniformly from the wall. Amplitude contours of the phase-averaged TS waves are shown in Figure 21 for phase interval one. Note the 180 degree phase shift between the waves above and below the critical layer. Not so obvious is the apparent merging of the TS waves in the inner region just downstream of the hole.

Two 3D data sets were obtained on four grids, totaling 79,560 data points each, for the cases without suction and with strong suction (V/U=0.36) applied to the hole. Here V is the bulk velocity through the hole and if this hole was embedded in a grid of holes of typical size, the suction coefficient would be $C_q \approx 15 \times 10^{-4}$. Multiple probes were used whenever possible to reduce the experimental run-time. A video animation of the results has been created.

A plan and side view of a positive and negative 3D contour surfaces (for phase one) of the TS waves in the vicinity of the hole are shown in Figure 22 for the case without net suction. Note the detailed "unfolding" of the narrow concentrated disturbances over the hole as the disturbances evolve downstream. The merging of the TS waves noted in the

centerline contours of Figure 21 have the appearance of slender "braids" in the 3D surfaces which appear to interconnect the surfaces.

A plan view of the contour surfaces for both cases (with suction and without suction) is shown in Figure 23. The evolution of TS waves appears to be much the same away from the centerline. However the behavior close to the centerline is different in each case. Without suction, the three-dimensionality on the centerline decays with streamwise distance and two-dimensional bow-shaped waves evolve further downstream. When suction is applied to the hole the three-dimensionality is much stronger and it does not decay as rapidly. The suction level is sufficiently high for the generation of two streamwise vortices from the hole but the spatial resolution of the probes is insufficient to resolve the details. However, further downstream, the TS waves exhibit spanwise clumps which could be the result of secondary instabilities associated with the suction hole vortices. Preliminary results were presented by Watmuff (1993).

Collaborations have been initiated with two computationalists who are interested in the Harmonic Point Source (HPS) problem i.e. the case without suction. Professor Thorwald Herbert from Ohio State University is working in conjunction with Dr. Les Mack of JPL on the HPS problem. Dr. Mack provided Linear Stability Theory (LST) calculations which appeared to contain many of the detailed features observed in the measurements. Herbert has developed Parabolized Stability Equation (PSE) methods. PSE is more realistic than classical linear stability theory (e.g. growth is accounted for in the streamwise direction) and it offers a significant advantage over DNS, since a typical run might take only take a few hours on a high performance work station. Herbert is also conducting a DNS investigation of the HPS corresponding to the experimental conditions without suction.

Mean flow and perturbation Plot3d files were reciprocally exchanged with Herbert and Mack via the Internet. The LST calculations have an overall appearance resembling the experimental data way from the centerline but contain significant differences in the vicinity of the disturbance. A major shortcoming of LST is that the distribution of the disturbance levels with y is not provided. The PSE results are in considerably better agreement with the experimental data but also fail to capture details near the centerline. The best comparison was observed with the DNS but there are also major differences on the centerline, especially near the origin of the disturbance. This is not surprising since the HPS was simulated by imposing a time varying velocity component normal to the wall. To date, the DNS simulations have been relatively crude since the time varying velocity boundary condition has been imposed at only a single grid point (see Mack and Herbert 1995). A better comparison with experimental data could result if a more sophisticated representation for the hole was used in conjunction with a finer grid. At this stage it is unknown whether the differences between the experiment and DNS are important for prediction purposes. However, one implication for DNS is that more sophisticated techniques could be required for modeling the disturbance at, or even within, the hole and potentially this could consume a significant proportion of valuable grid resources.

2.4.3 Interactions between Disturbances Generated at Two Holes

Interaction between TS waves generated by multiple holes, displaced, but aligned in the streamwise direction is of considerable importance because of the possibility of cancellation (or enhancement) of disturbances. Much attention has been given to the *cross-stream* layout of the grid of suction holes (Goldsmith's Correlation) but almost no attention has been paid to the *streamwise* layout of the grids. Consideration has been given to suction hole vortices but no attention has been made to TS waves generated by the holes. Initial observations concerning the possibility of TS wave cancellation were performed using the centerline pressure tap holes of the impervious plate which was used to establish the base flow. Unfortunately the distance between successive pressure taps is about three TS wavelengths. The spanwise propagation of the waves between successive holes is too large to provide a dramatic demonstration of the cancellation. However the tests were successful for demonstrating the linearity of the TS wave interaction which is an underlying requirement for wave cancellation.

Three series of tests were performed using two holes. In the first test the harmonic disturbance was applied only to the first hole. In the second test the disturbance was applied only to the second hole and in the third test the same disturbance was applied to both holes simultaneously. The same spatially dense 3D measurement grid was used in all cases. To demonstrate the linearity, the measured perturbations generated by the first hole acting alone were numerically added to the measured perturbations generated by the second hole acting alone. The results constructed from the two sets of independent measurements appeared almost identical to the measurements obtained when the disturbance was applied to both holes simultaneously.

On the basis of these observations, the possibility of TS wave cancellation was demonstrated using a single set of measurements. Perturbations originating from a second hole located one TS wavelength downstream were *simulated* by associating the measured perturbations with grid points located downstream. The interaction between disturbances originating from the original hole and the simulated hole was studied by numerically adding the perturbations. The results of the simulation are shown in Figure 24. No attempt was made to interpolate the data in the region of overlap of dissimilar grids caused by the streamwise displacement. These regions have been left blank in the Figures.

The wave cancellation in the vicinity of the holes was only minimal owing to the rapid evolution in these regions. However, further downstream in the region where the waves become more bow-like, the cancellation of TS waves was extensive as shown in Figure 24(c).

This results of the simulation implies that an optimal streamwise hole spacing could exist for cancellation of TS waves. The optimum hole spacing would be a function of the flow speed (i.e. TS wavelength). An unfortunate flight speed and hole spacing combination could even lead to TS wave enhancement and defeat the purpose of the suction i.e. cause earlier transition. Furthermore, nothing is known about the inevitable interaction between TS waves and suction hole vortices which could also be detrimental.

3. DESIGN AND FABRICATION OF NEW HIGH-PERFORMANCE CONSTANT-TEMPERATURE HOT-WIRE ANEMOMETERS

New high performance constant temperature hot-wire anemometers have been developed for general purpose use in the Fluid Mechanics Laboratory, Watmuff (1994). The design is based on results presented in a series of papers i.e. Watmuff (1987), Watmuff (1988), Watmuff (1989) and Watmuff (1990). Twenty-eight instruments have been delivered, at a cost of around $1K each. The performance is equal to or superior to commercially available instruments costing $10K each. Nine of these instruments were used in this project.

The design is based on a linear system theory analysis that can be extended to arbitrary order. A motivating factor was to achieve the highest possible frequency response while ensuring overall system stability. Based on these considerations, the design of the circuit and the selection of components is discussed in depth. Basic operating instructions are included in an operator's guide. The analysis is used to identify operating modes, observed in all anemometers, that are misleading, in the sense that the operator can be deceived by interpreting an erroneous frequency response. Unlike other anemometers, this instrument provides front panel access to all the circuit parameters which affect system stability and frequency response. Instructions are given on how to identify and avoid these rather subtle and undesirable operating modes by appropriate adjustment of the controls. Details, such as fabrication drawings and a parts list, are provided in Watmuff (1994). The analysis and examples of system response have also been accepted for publication, Watmuff (1995b).

ACKNOWLEDGMENTS

All experiments were performed in the Fluid Mechanics Laboratory Branch (FML) at NASA Ames Research Center. The Laminar Separation/Turbulent Reattachment study was started during the last two months of support as a Research Fellow with the NASA/Stanford CTR. Primary funding for construction of the wind tunnel modifications for the Suction Hole Studies was obtained via Director's Discretionary Funds (DDF) in collaboration with Dr. Daniel C. Reda. The author wishes to thank Dr. J.M. Kendall and Dr. L.M. Mack of JPL and Professor T. Herbert of Ohio State University for many fruitful discussions with respect to the Harmonic Point Source data.

REFERENCES

CURLE, N. & SKAN, S.W. 1957 Approximate methods for predicting separation properties of laminar boundary layers. *Aero. Q.* **8,** 257-268.

GASTER, M. & GRANT, I. 1975 An experimental investigation of the formation and development of a wave packet in a laminar boundary layer. *Proc. Roy. Soc.* **A347,** 253-269.

MACK, L.M. & HERBERT, T. 1995 Linear wave motion from concentrated harmonic point sources in Blasius flow. *AIAA* Paper No. **95-0774.**

MICHALKE, A. 1964 On the inviscid instability of the hyperbolic-tangent velocity profile. *J. Fluid Mech.* **19**, 543-556

MONKEWITZ, P.A. & HUERRE, P. 1982 Influence of the velocity ratio on the spatial stability of mixing layers. *Phys. Fluids* **25**, 1137-1143

SPALART, P. R. & WATMUFF, J.H. 1993 An Experimental and numerical study of a turbulent boundary layer with pressure gradients. *J. Fluid Mech.* **249,** 337-371.

WATMUFF, J.H. 1987 Higher order effects in the frequency response of the constant temperature hot-wire anemometer. *ASME Applied Mechanics, Bioengineering and Fluid Mechanics Conference,* FED-Vol. **53**, 25-34.

WATMUFF, J.H. 1988 Increasing the frequency response of constant temperature hot-wire anemometer systems for use in supersonic flow. *AIAA* Paper No. **88-0421.**

WATMUFF, J.H. 1989 The effects of feedback amplifier characteristics on constant temperature hot-wire anemometer systems. *Tenth Australasian Fluid Mechanics Conference*, Paper **15D-1**, 15.33.

WATMUFF, J.H. 1990 Tuning the constant-temperature hot-wire anemometer. *ASME Symposium on Heuristics of Thermal Anemometry*, FED-Vol. **97**, 17-22.

WATMUFF, J.H. 1991a, Phase-averaged measurements of perturbations introduced into boundary layers. *CTR, Ann. Res. Briefs* - 1990. Stanford University.

WATMUFF, J.H. 1991b An experimental investigation of boundary layer transition in an adverse pressure gradient. *ASME Symposium on Boundary Layer Stability and Transition to Turbulence*, FED-Vol. **114**, 129-136.

WATMUFF, J.H. 1993 Interaction between instabilities originating from suction holes. *Bull. of Amer. Phys. Soc.*, Vol. 38, **12**, 2237.

WATMUFF, J.H. 1994a, A new high performance constant temperature hot-wire anemometer. *NASA Contractor Report* **177645.**

WATMUFF, J.H. 1994b, Instabilities originating from suction holes used for laminar flow control. *MCAT Inst. Progress Report* **94-23**, July 1994.

WATMUFF, J.H. 1995a, High-speed real-time processing of cross-wire data. *Exp. Thermal and Fluid Sci. J.*, **10**, 75-85.

WATMUFF, J.H. 1995b, An Investigation of the Constant-Temperature Hot-Wire Anemometer. Accepted for publication, *Exp. Thermal and Fluid Sci. J.*

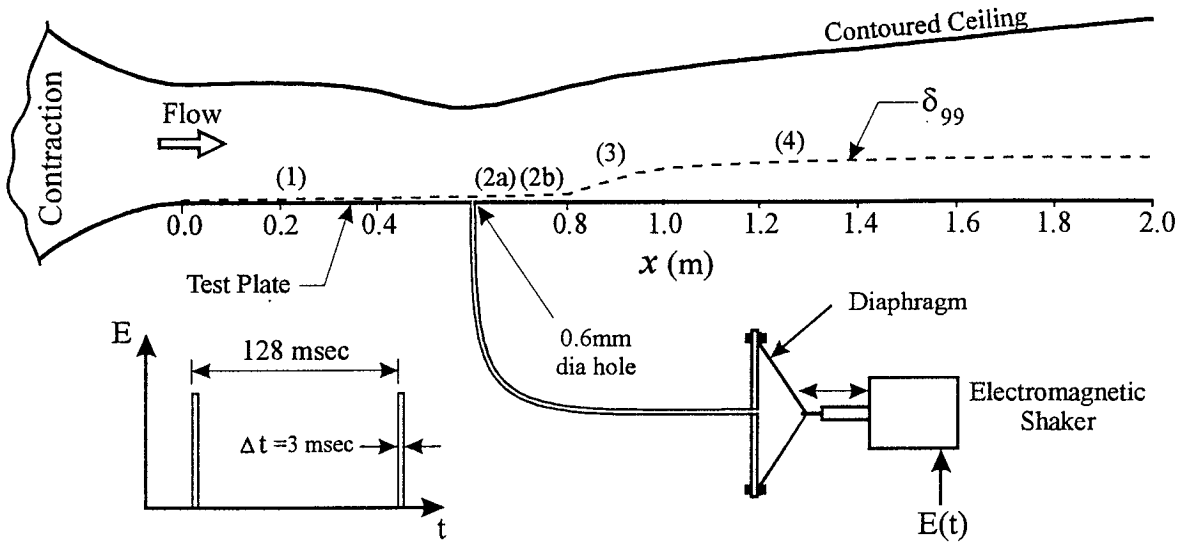

Figure 1. Scaled side view of 1m wide test section for laminar separation/turbulent reattachment studies with schematic showing method for insertion of disturbance at the C_p minimum. Flow regimes:
(1) Development of laminar boundary layer in FPG ($0 < x < 0.60$m)
(2a) Layer separates in APG, decay of disturbance generated wave packet ($0.60\text{m} < x < 0.68$m)
(2b) Separated layer in APG, linear growth of dispersive wave packet ($0.68\text{m} < x < 0.80$m)
(3) Reattachment, wave packet evolves into vortex loops ($0.80\text{m} < x < 1.10$m)
(4) Fully turbulent boundary layer, vortex loops retain identity ($1.10\text{m} < x < 2.00$m)

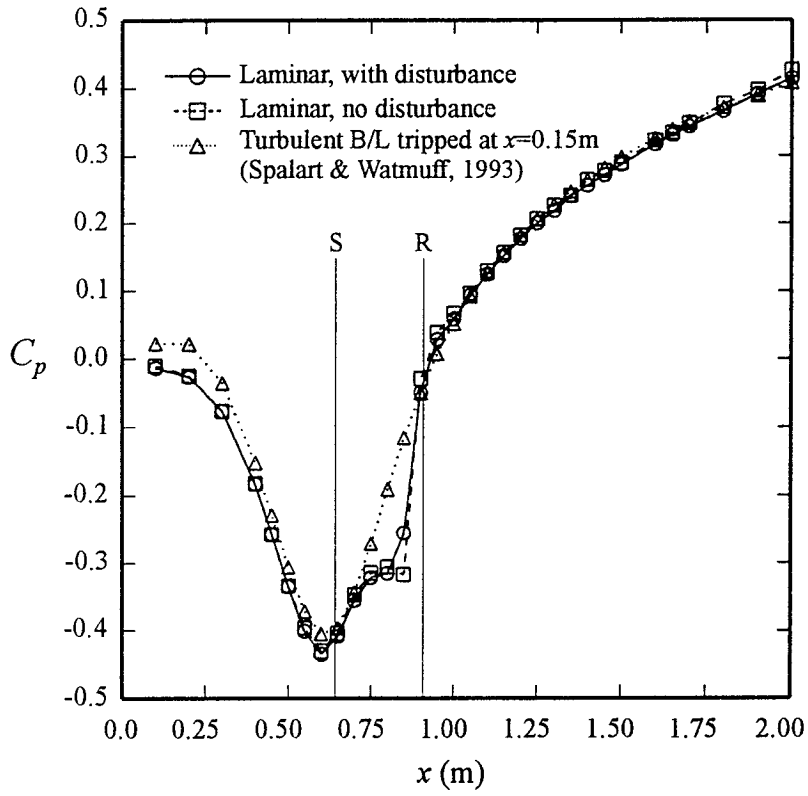

Figure 2. Centerline C_p distribution for two conditions in laminar separation/turbulent reattachment study. Also shown is C_p for turbulent layer, tripped in FPG, which remains attached. S indicates separation and R reattachment points without disturbance.

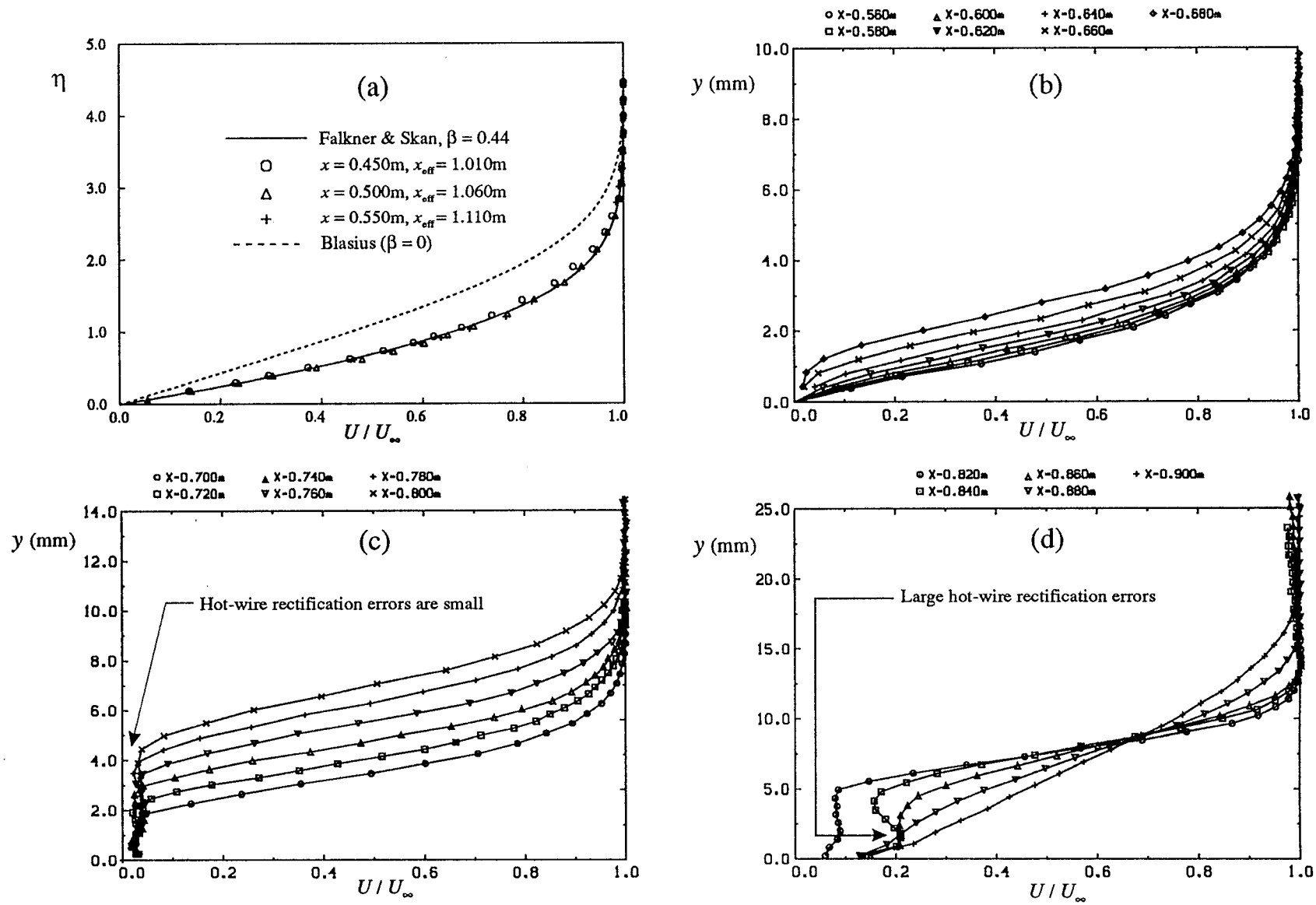

Figure 3. Centerline mean velocity profiles (using stationary hot-wire).
(a) FPG data in Falkner & Skan coordinates using an effective origin (x_{eff} =0, x= - 0.56m) compared to similarity solution using approximately constant experimental value β=0.44 in this region (Blasius also shown).
(b) APG region 2a (amplitude of disturbance generated wave packet decays with x)
(c) APG region 2b (spanwise propagation of waves and exponential growth of amplitude with x)
(d) Reattachment region 3, and start of region 4 (Large hot-wire rectification errors due to increased unsteadiness).

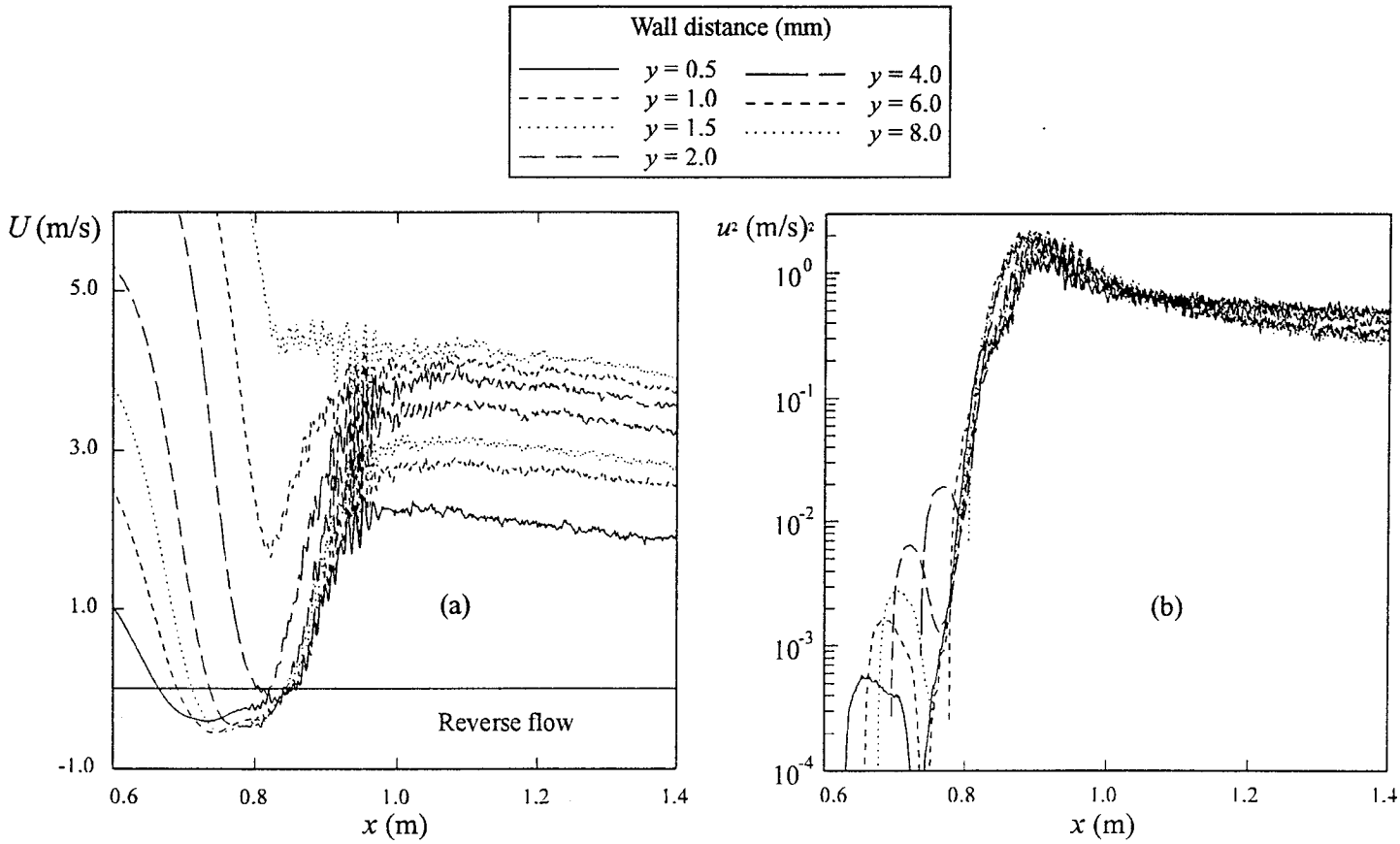

Figure 4. Flying hot-wire (U_{wire} = -1.5 m/s) measurements along centerline streamwise trajectories at various wall distances. Streamwise interval between data points is 1mm with 500 samples (upstream passes) at each point (a) Mean velocity relative to a stationary observer (b) Mean square of fluctuations.

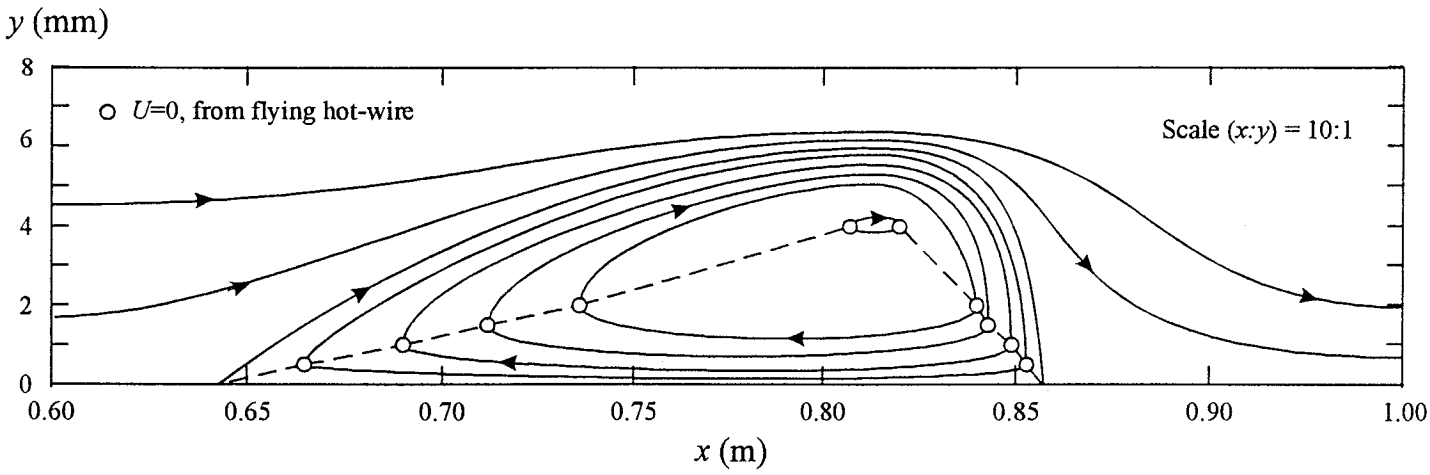

Figure 5. Plausible temporal mean streamline pattern of separation bubble deduced from points U=0 in flying hot-wire measurements (streamline $dy/dx=\infty$). Extrapolation to the wall to estimate temporal mean separation point on centerline at x=0.64m and reattachment at x=0.86m.

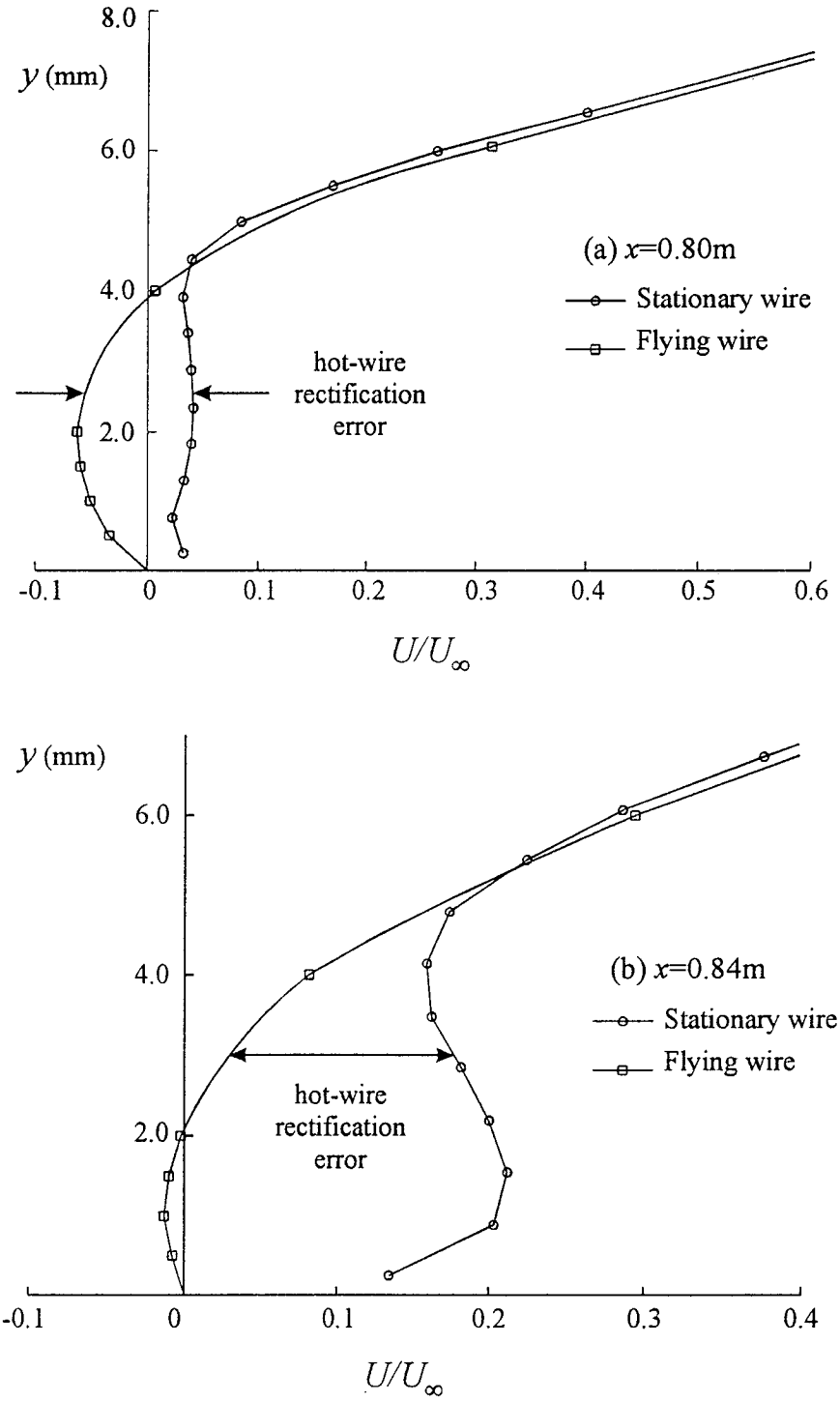

Figure 6. Comparison of inner region of stationary and flying hot-wire profiles. Within bubble approaching reattachment (a) x=0.80m, relatively small amplitude fluctuation levels cause region affected by rectification errors to coincide approximately with reversed flow (b) x=0.84m, large fluctuations increase relative size of region affected by rectification errors. Sparse flying wire data points joined by faired curves.

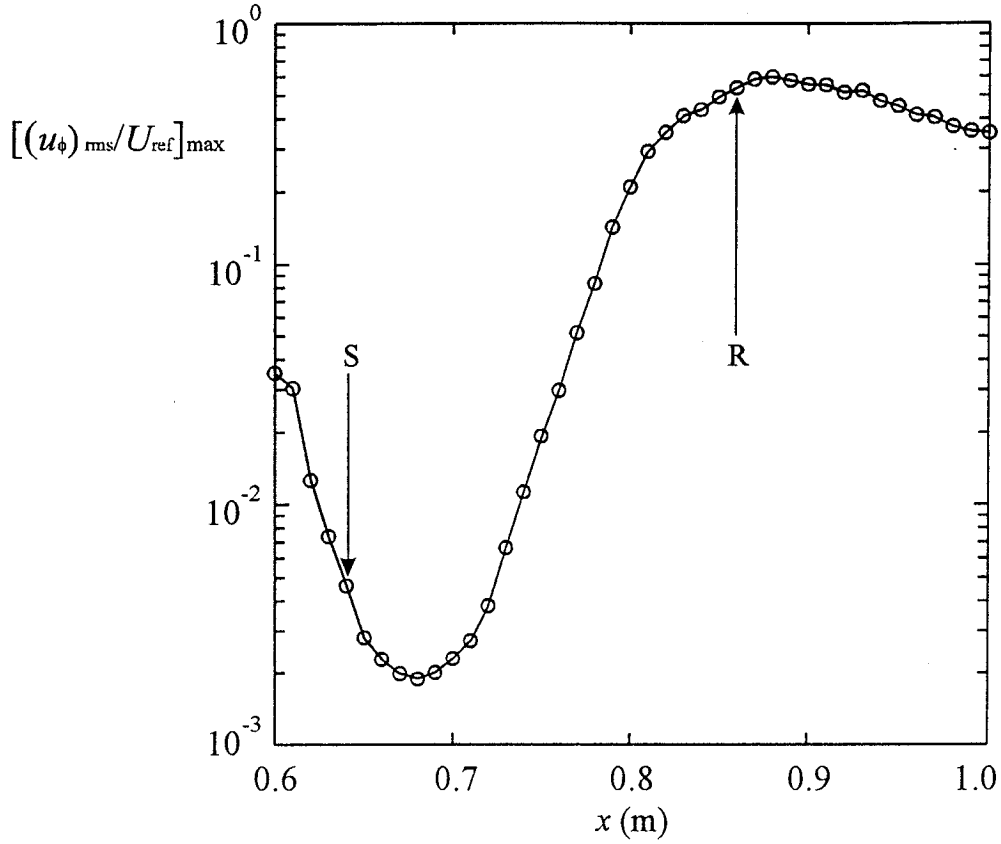

Figure 7. Development of maximum rms amplitude of phase-averaged perturbation in each yz-plane (Ny, Nz)=(17,11) spaced at 10mm intervals in x. S indicates separation and R reattachment points.

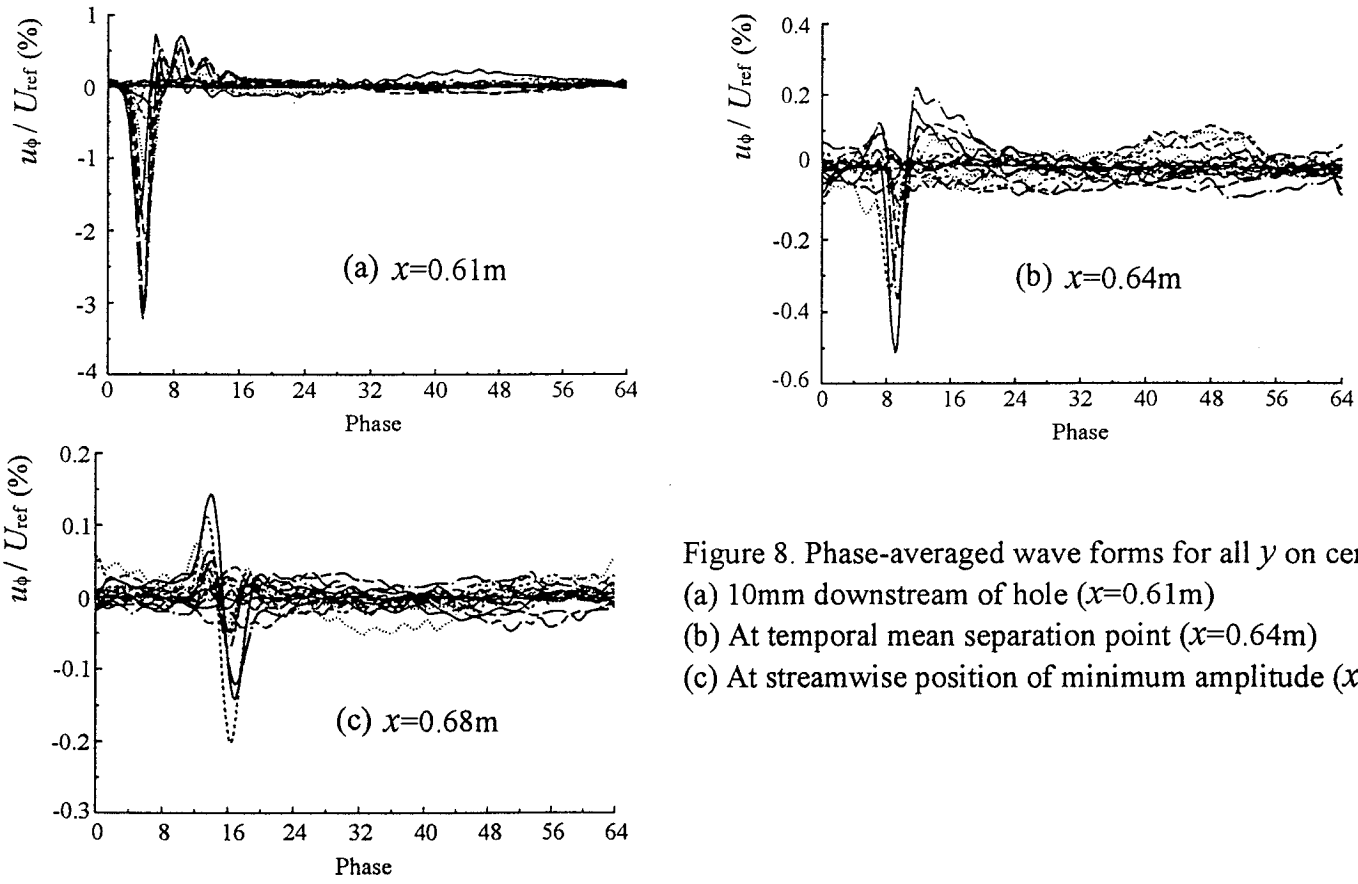

Figure 8. Phase-averaged wave forms for all y on centerline.
(a) 10mm downstream of hole (x=0.61m)
(b) At temporal mean separation point (x=0.64m)
(c) At streamwise position of minimum amplitude (x=0.68m)

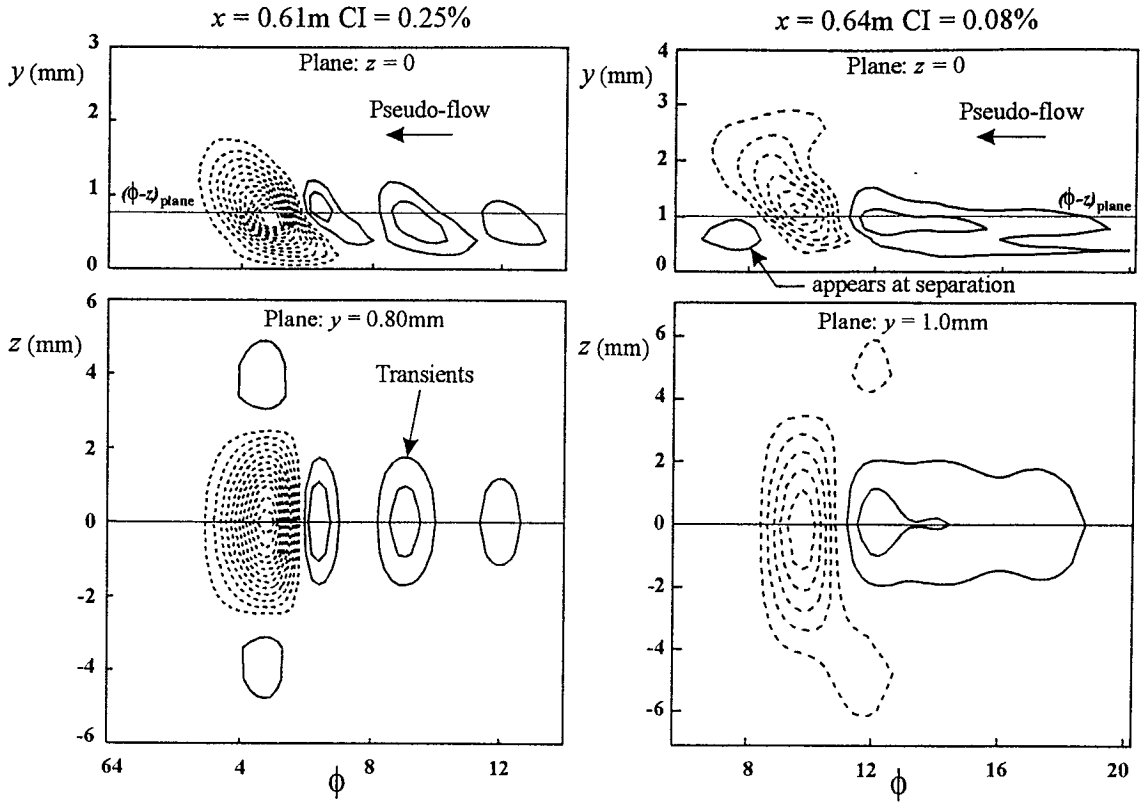

Figure 9. Development of contours of phase-averaged perturbation u_ϕ/U_{ref} in attached layer. Phase (ϕ) applied as third coordinate to data in y-z plane (pseudo-flow visualization). The overall perturbation shape remains much the same in this region of exponential decay. CI is contour increment, solid lines are positive and dashed lines are negative levels.

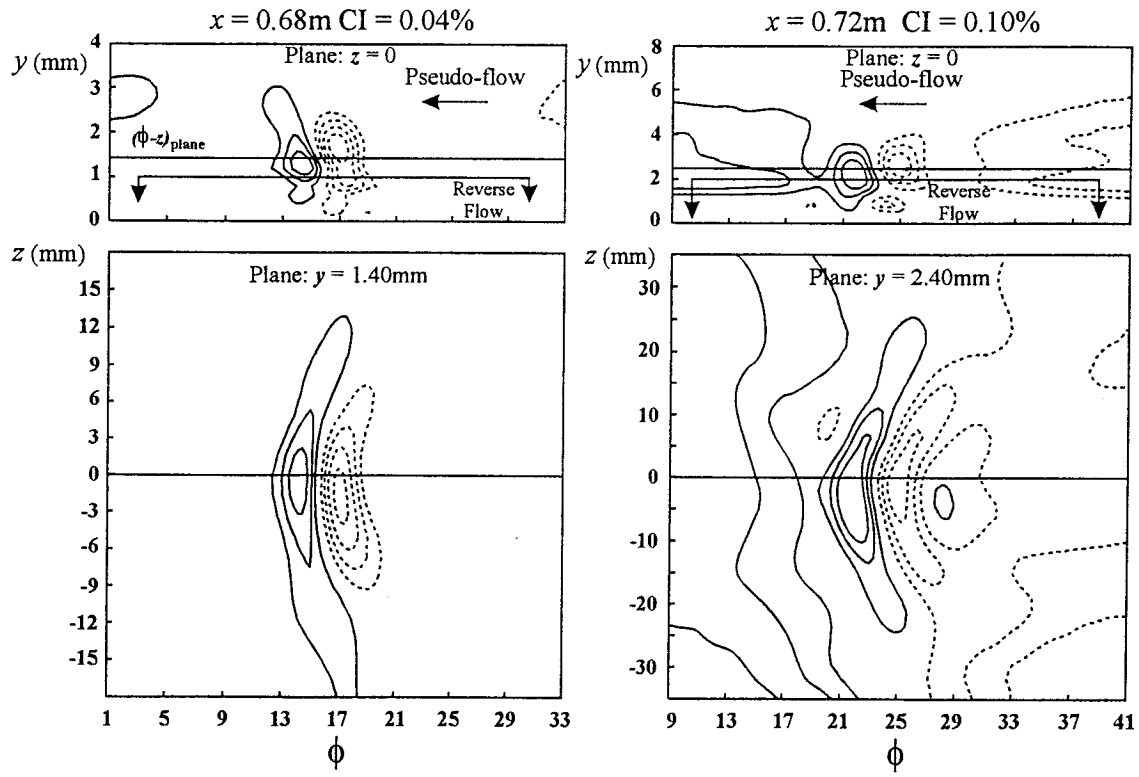

Figure 10. Pseudo-flow visualization contours showing development of dispersive wave characteristics in region of growth from x=0.68m (minimum rms level) to x=0.72m (start of region with exponential growth rate with x).

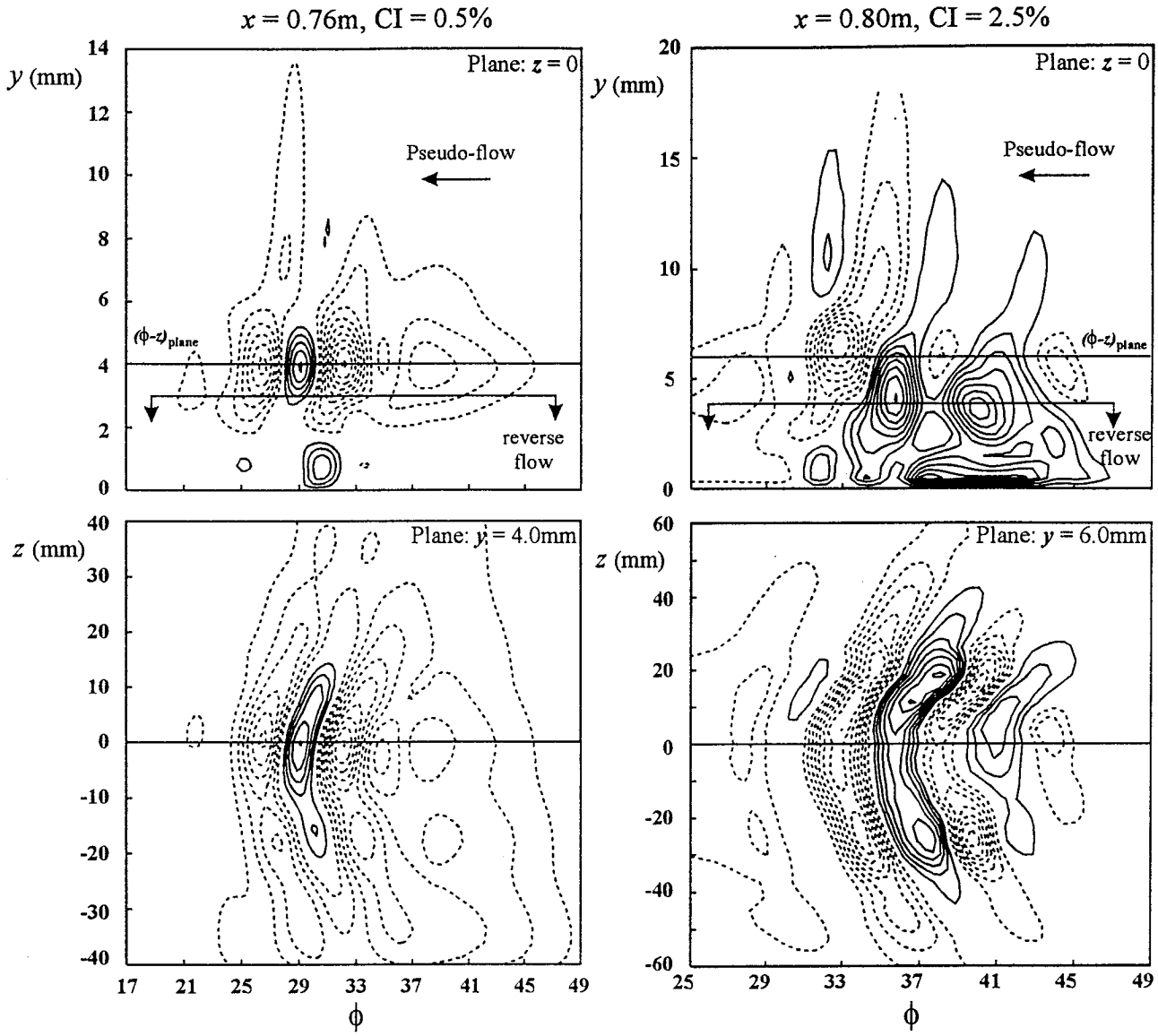

Figure 11. Pseudo-flow visualization contours of waves in region of exponential growth rate with x.

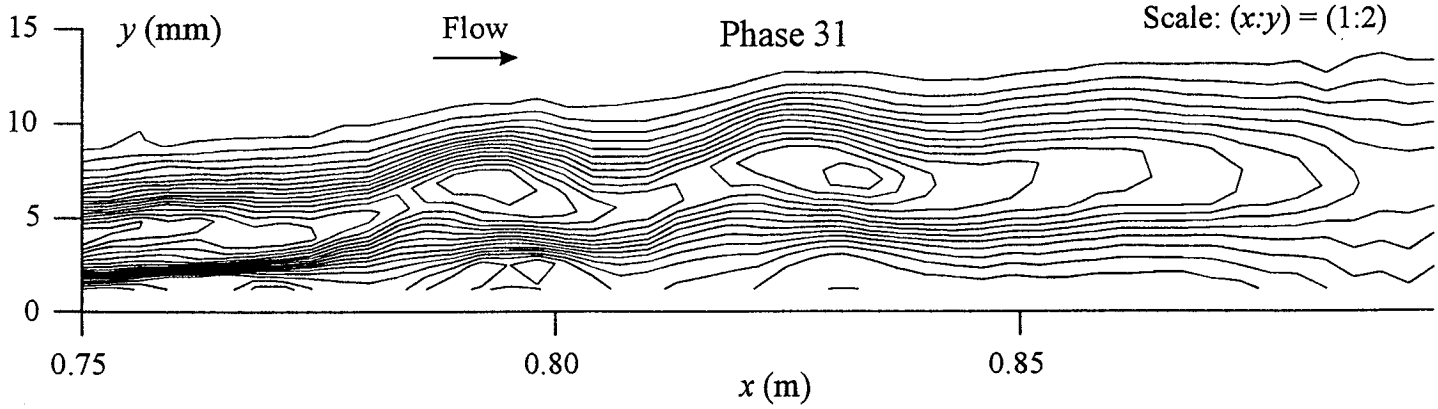

Figure 12. True spatial flow visualization contours of phase-averaged spanwise vorticity for phase 31 calculated from cross-wire data on centerline plane. Waves observed in figure 11 are associated with the formation of Kelvin-Helmholz "cats-eye" pattern in detached shear layer. Flow is left to right. CI= 100 rad/s.

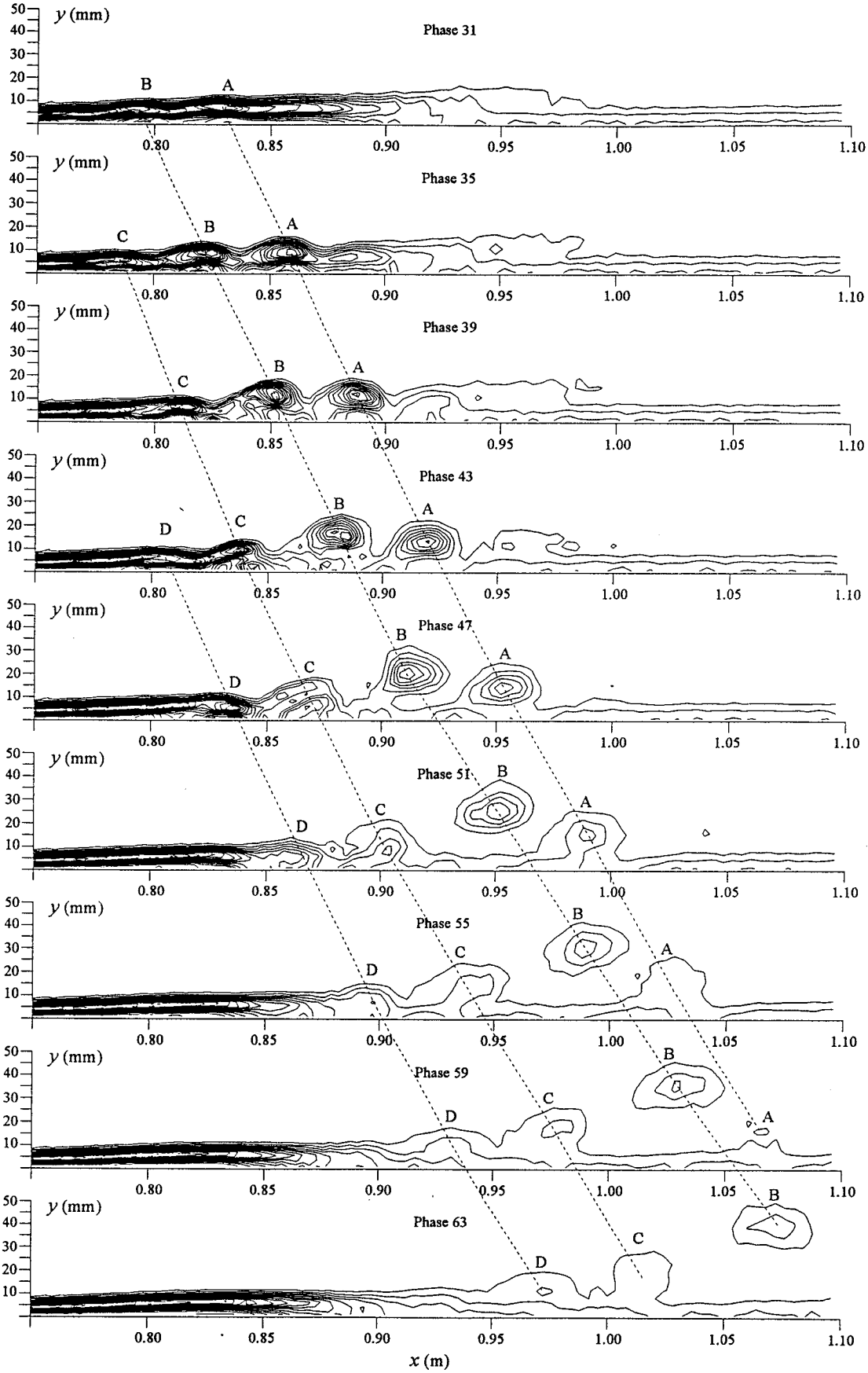

Figure 13. Animation sequence of spanwise vorticity contours on centerline plane calculated from cross-wire data. Dashed lines trace the development of roll-ups into vortex loops. The first distinct roll-up (labeled A) appears short-lived, while it is the second roll-up (labeled B) that accelerates away and evolves into the largest vortex loop (also see Figure 14). Vortex loop B is identifiable downstream in the fully turbulent layer (see Figure 17) . CI=100 rad/s.

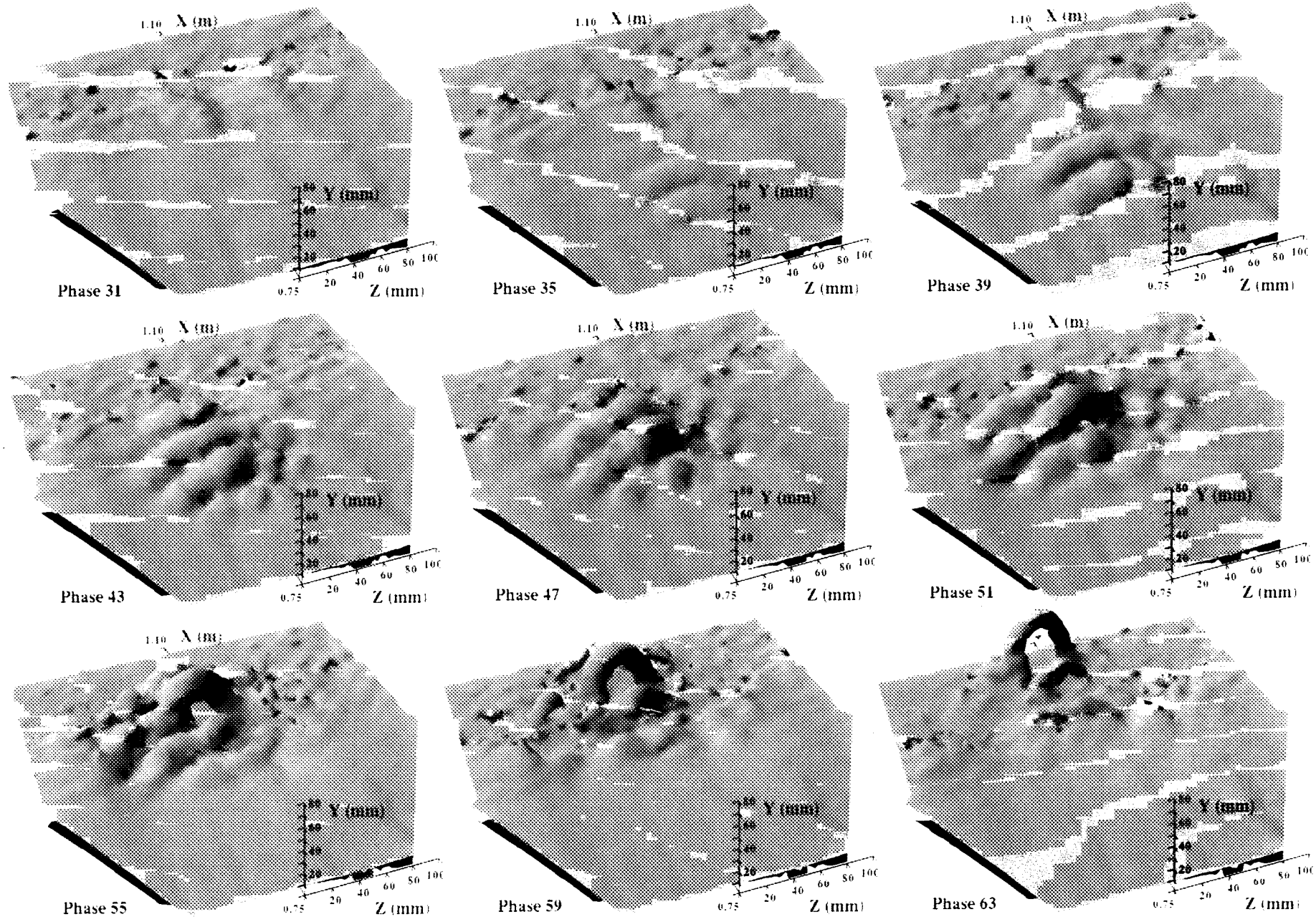

Figure 14.Animation sequence of 3D contour surface of phase-averaged vorticity magnitude=140 rad/s, calculated from cross-wire data on $(N_x, N_y, N_z) = (45, 17, 41)$ grid, measured twice, to get all three velocity components. The development of 3D waves on the surface and the subsequent roll-up to form vortex loops is clear on the centerline. Smaller loops can also be seen off centerline e.g. $z < 0$ for phase 55.

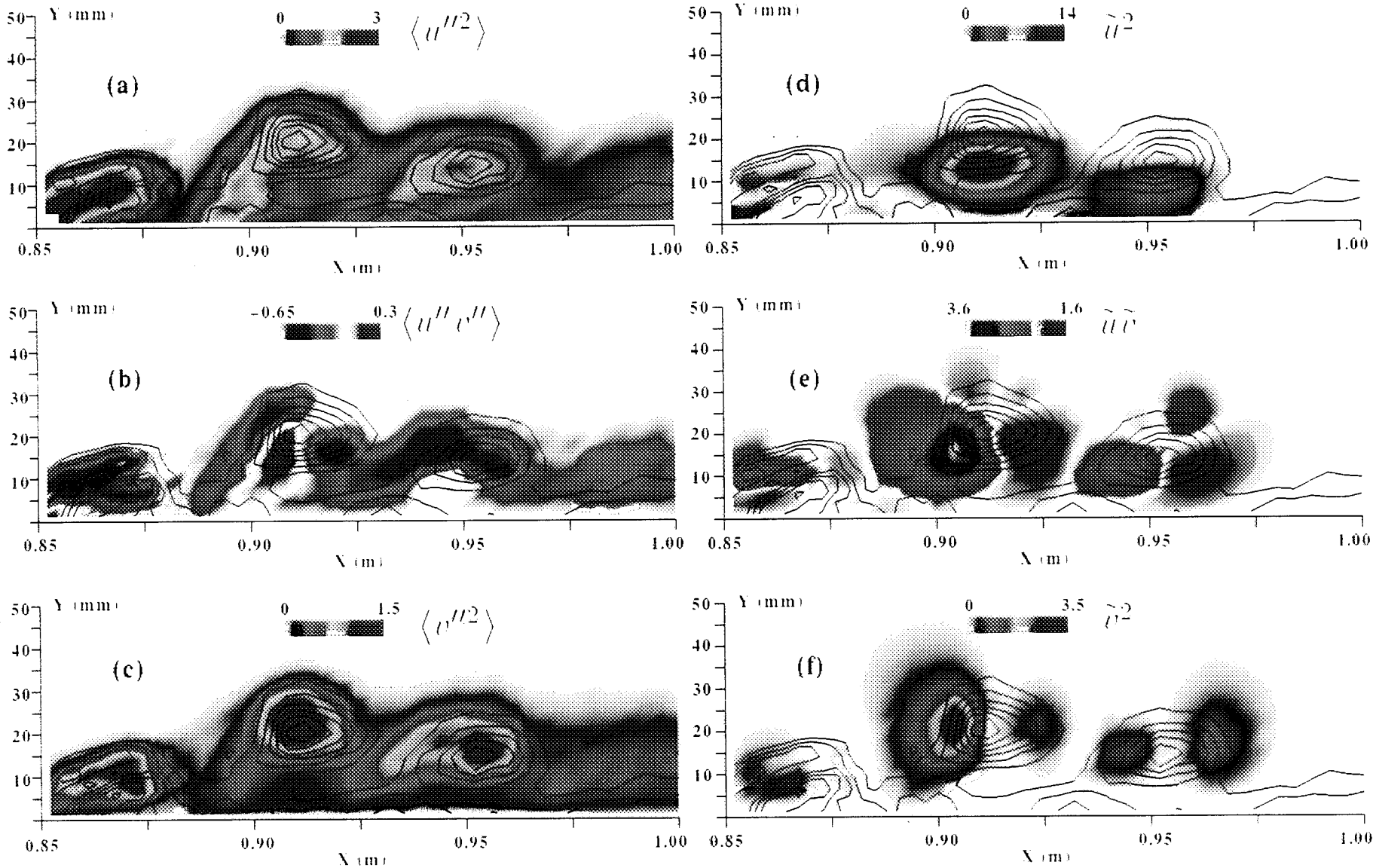

Figure 15. Color contours of the Contribution to the Reynolds stress by the phase-averaged velocity fluctuations (a), (b) and (c), and the Background Reynolds stress due to random velocity fluctuations (d), (e) and (f) (see Watmuff 1991b, for notation). Centerline plane for Phase 47. Solid lines are the corresponding phase-averaged spanwise vorticity contours. CI=100 rad/s.

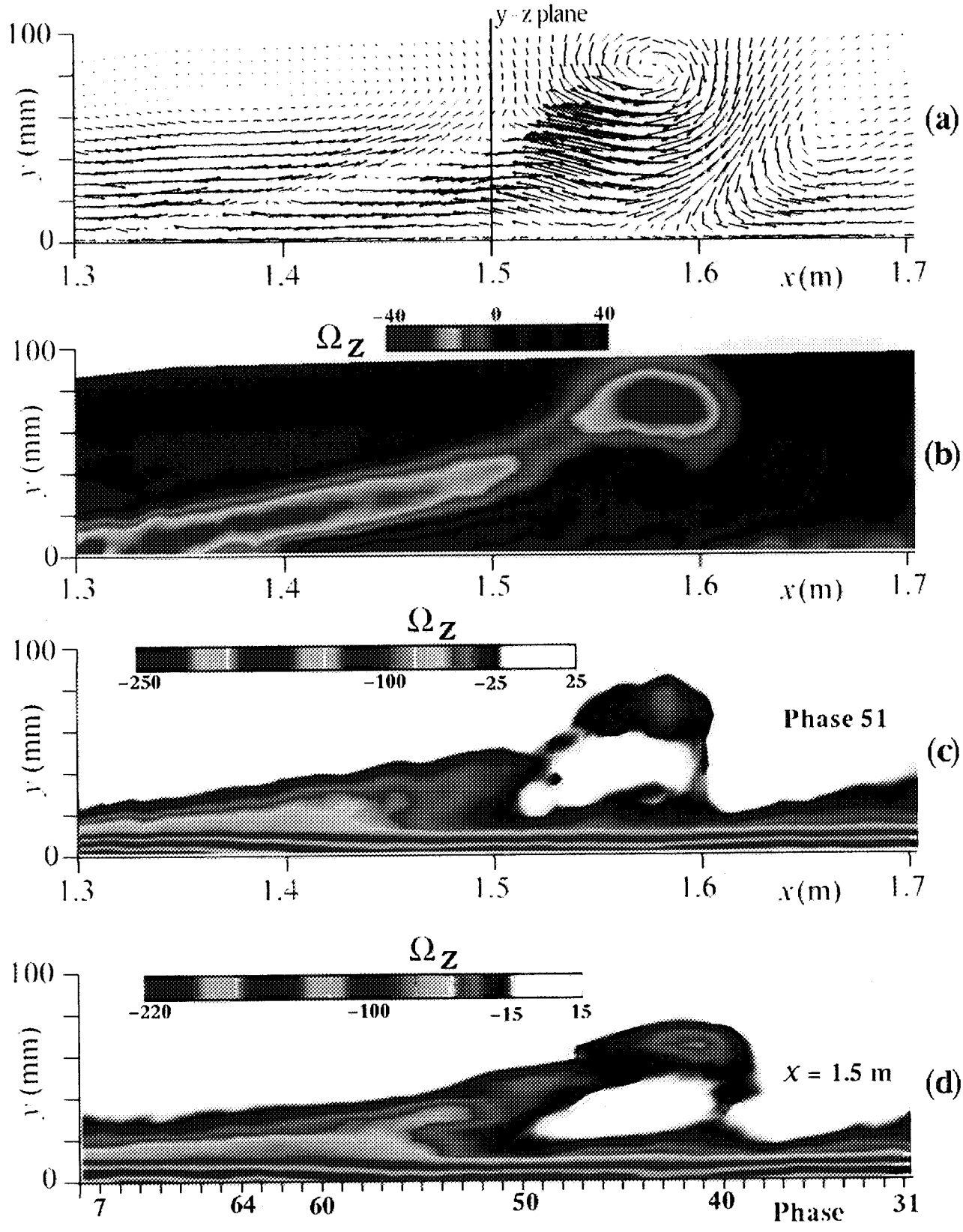

Figure 16. (a) Phase-averaged velocity perturbation vector field (b) corresponding spanwise vorticity perturbation contours (c) corresponding total spanwise vorticity contours (d) spanwise vorticity contours derived by applying Taylor's hypothesis for phase to centerline data of spanwise plane at x=1.5m.

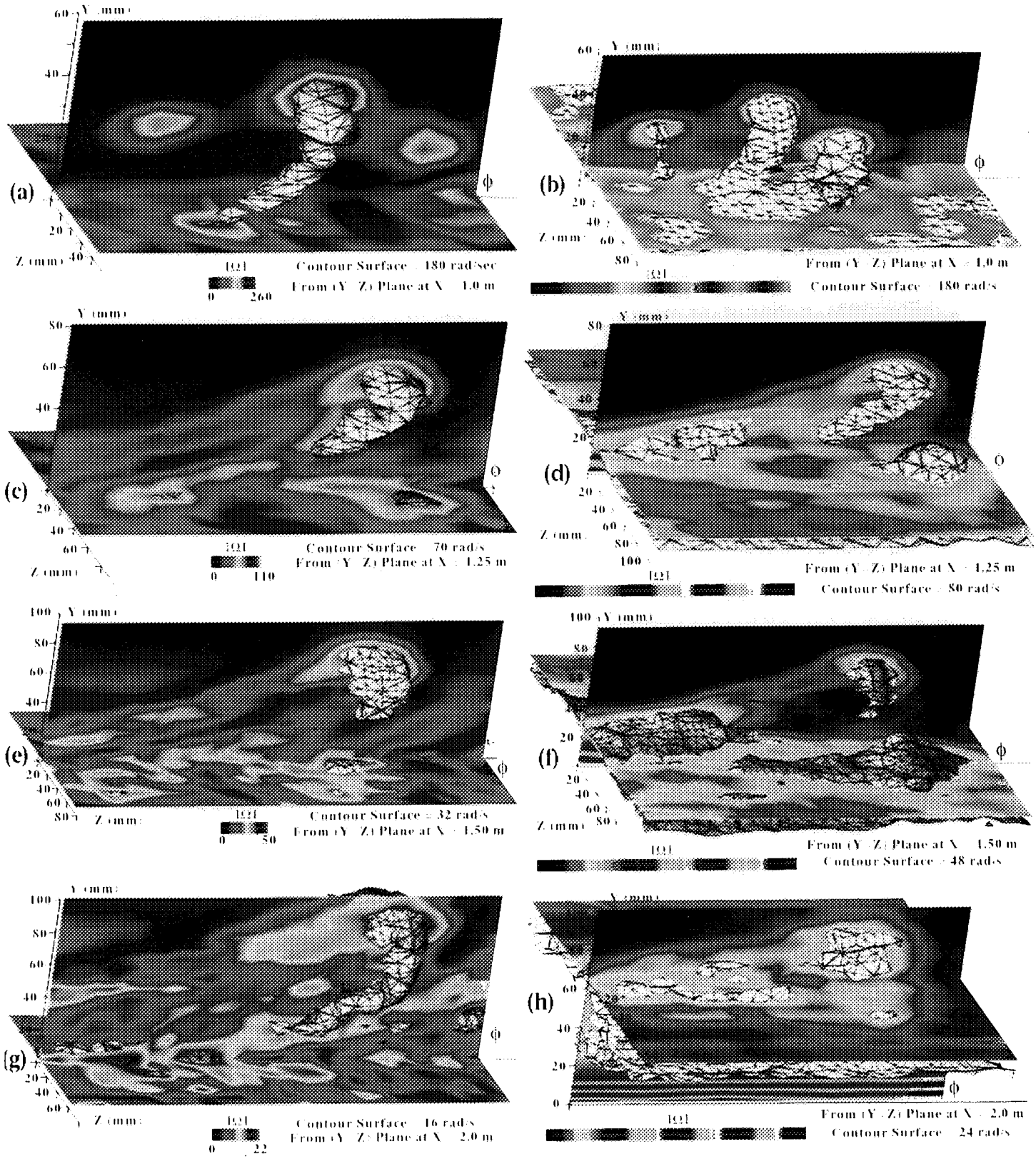

Figure 17. Vorticity magnitude derived by applying Taylor's hypothesis for phase to spanwise planes for generation of 3D velocity field. Contour surface and contours on centerline plane and plane normal to wall. (a) & (b) x=1.0m, (c) & (d) x=1.25m, (e) & (f) x=1.5m and (g) & (h) x=2.0m. Vorticity magnitude perturbations in (a), (c), (e) & (g). Total vorticity magnitude in (b), (d), (f) & (h).

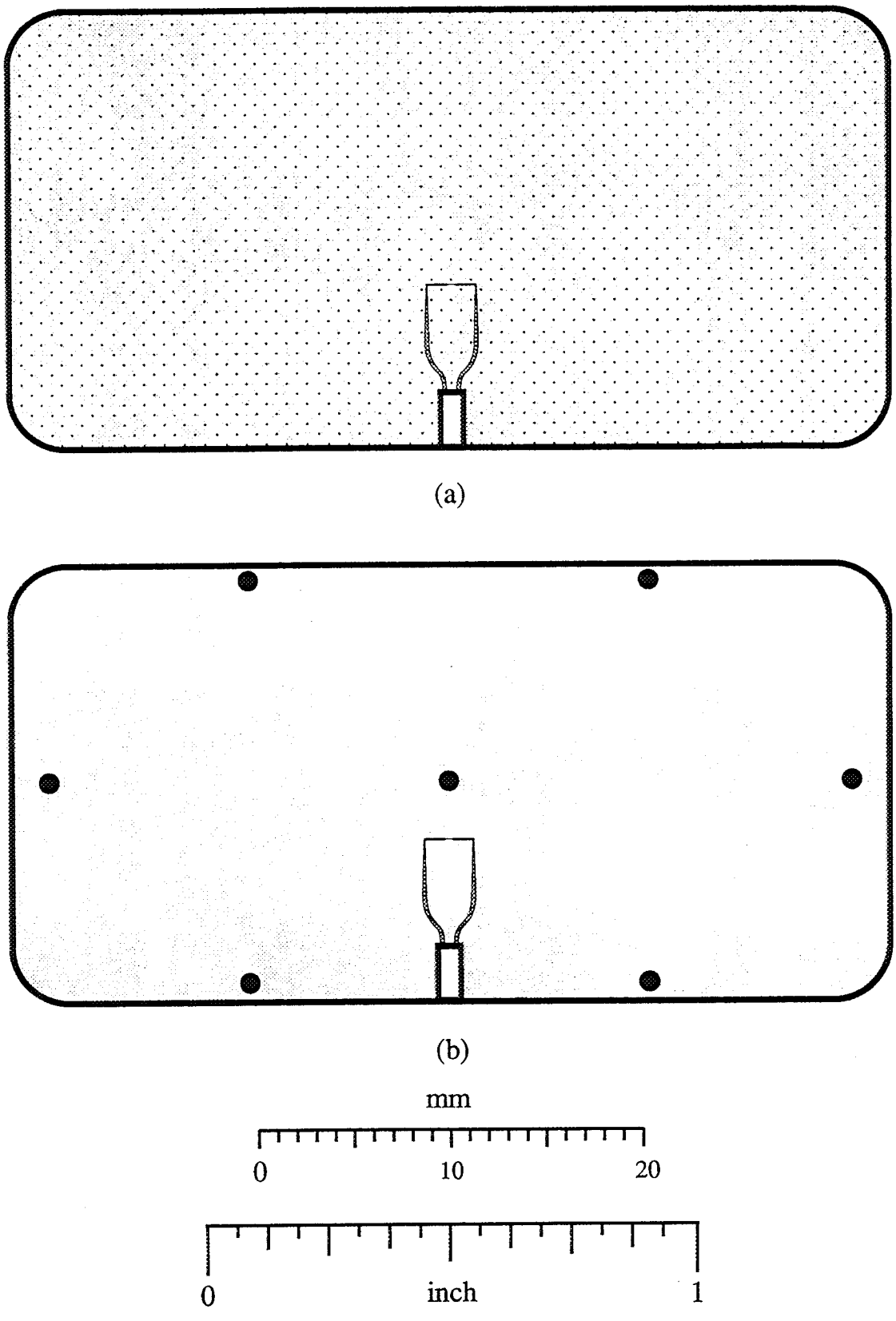

Figure 18. Relationship between size of suction holes and normal hot-wire probe with 0.5mm long sensor. (a) Typical "laser-drilled" porous surface used in flight tests. (b) Typical porous surface scaled up by a factor of 20:1 for improved spatial resolution with hot-wires.

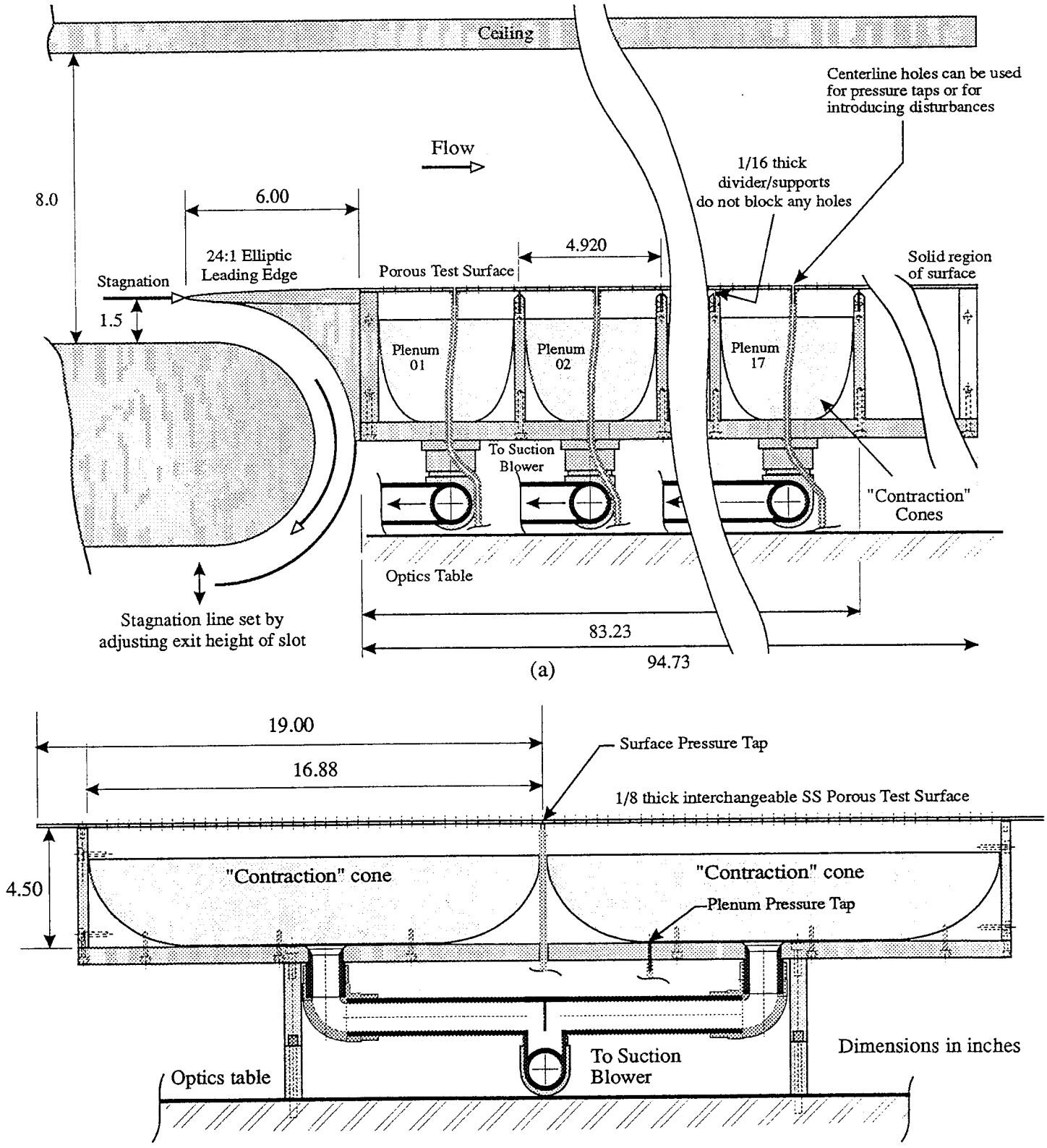

Figure 19. Layout of interchangeable porous surface assembly in test section. Stagnation line on leading edge is set by adjusting the exit height of the slot. Plenum chambers with bath-tub shaped contraction cones gather flow through porous surface into tubes connected to high pressure blower providing the suction. (a) Longitudinal section through centerline of test section. (b) Cross section through a plenum chamber.

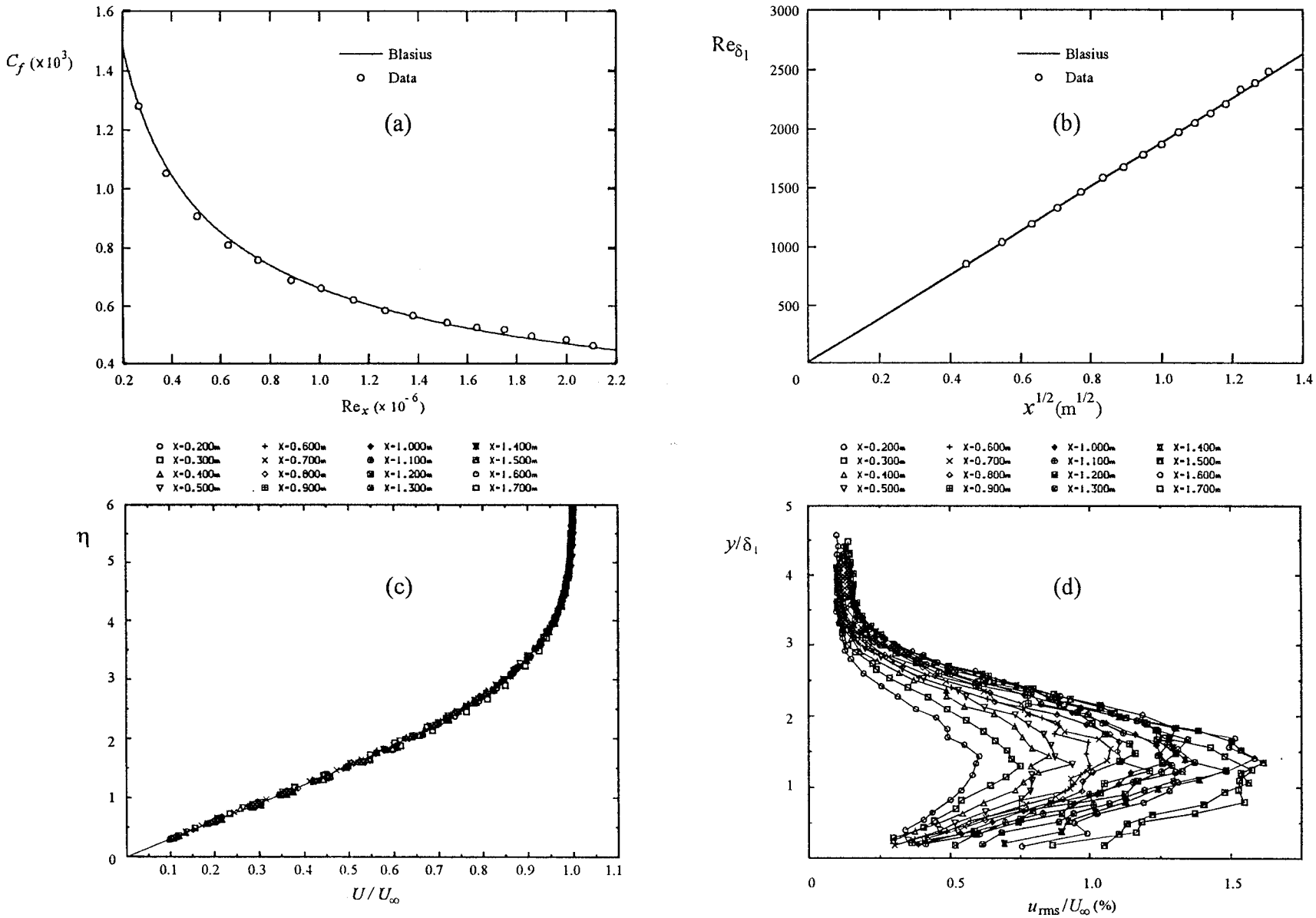

Figure 20. Mean flow properties of base flow (a) skin friction derived from velocity gradient at wall (b) displacement thickness (c) mean velocity profiles in Blasius coordinates, and (d) rms fluctuations.

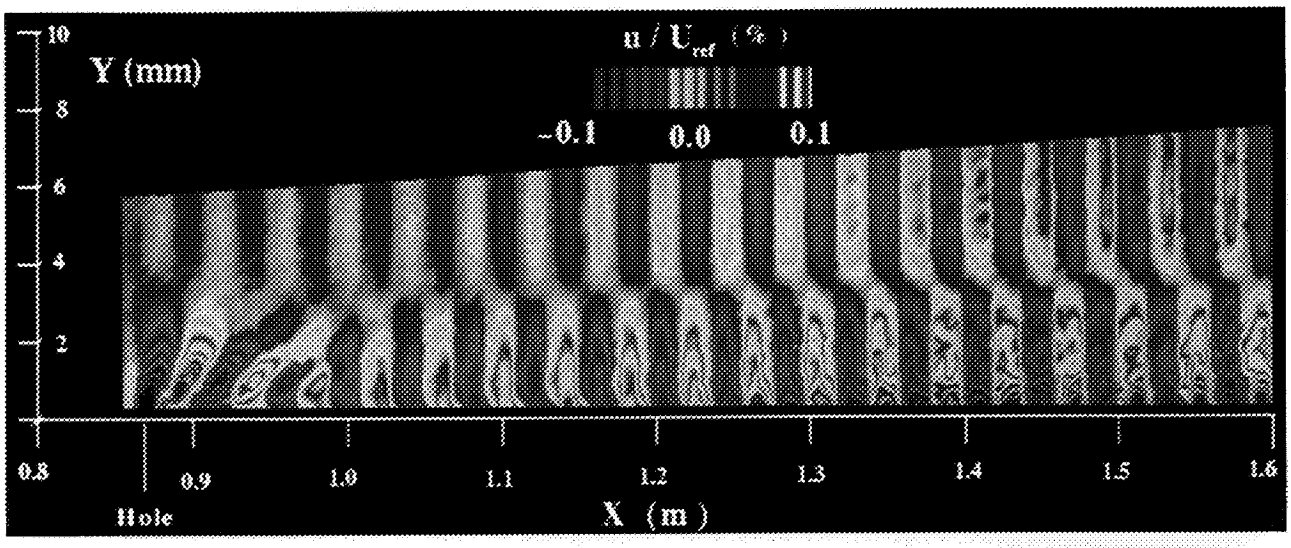

Figure 21. Contours of TS waves in centerline plane for case with no net suction.

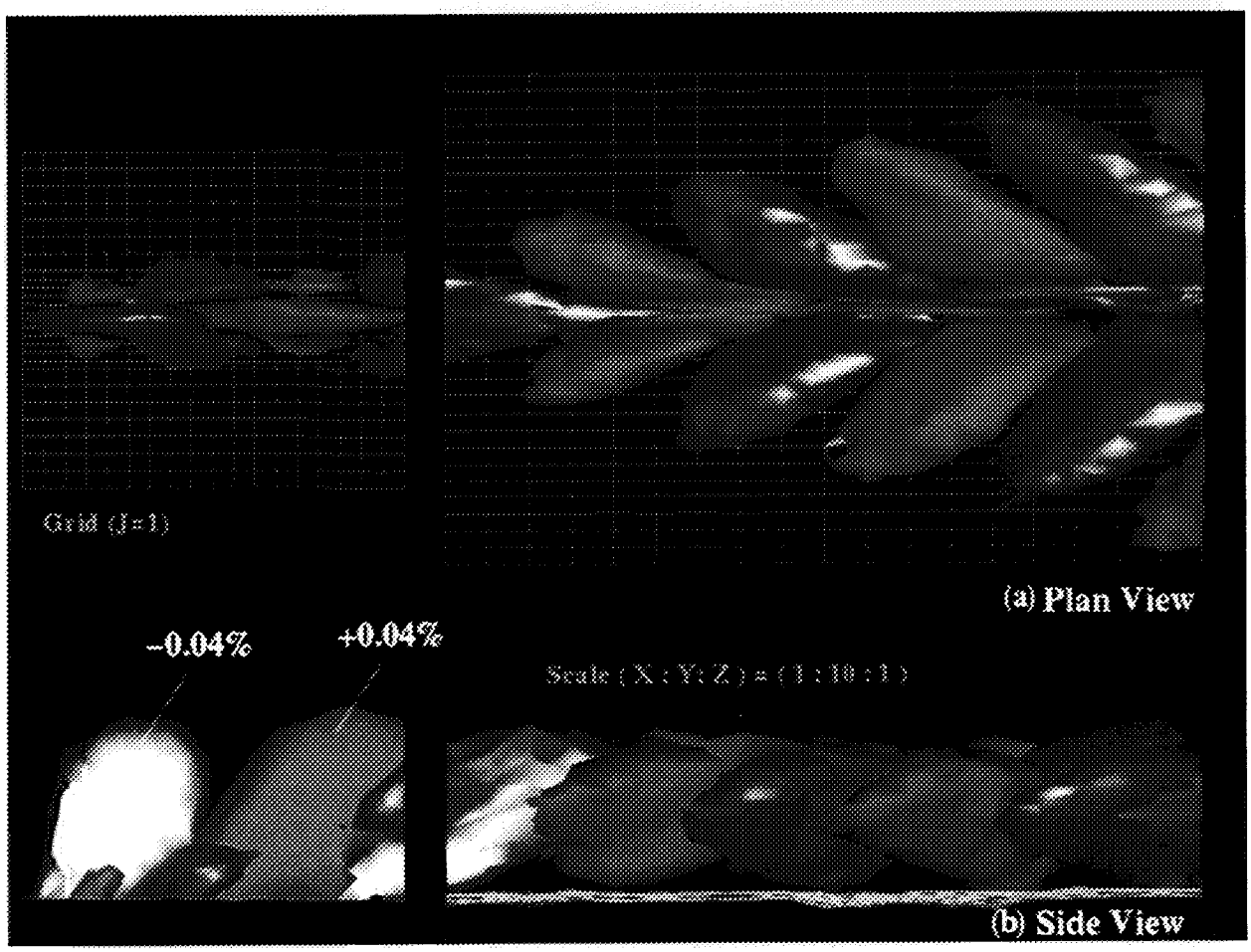

Figure 22. Closeup showing evolution of 3D contour surfaces (±0.04%) of phase-averaged TS waves in vicinity of hole for no net suction. Note "braids" interconnecting surfaces on centerline. (a) plan view (b) side view.

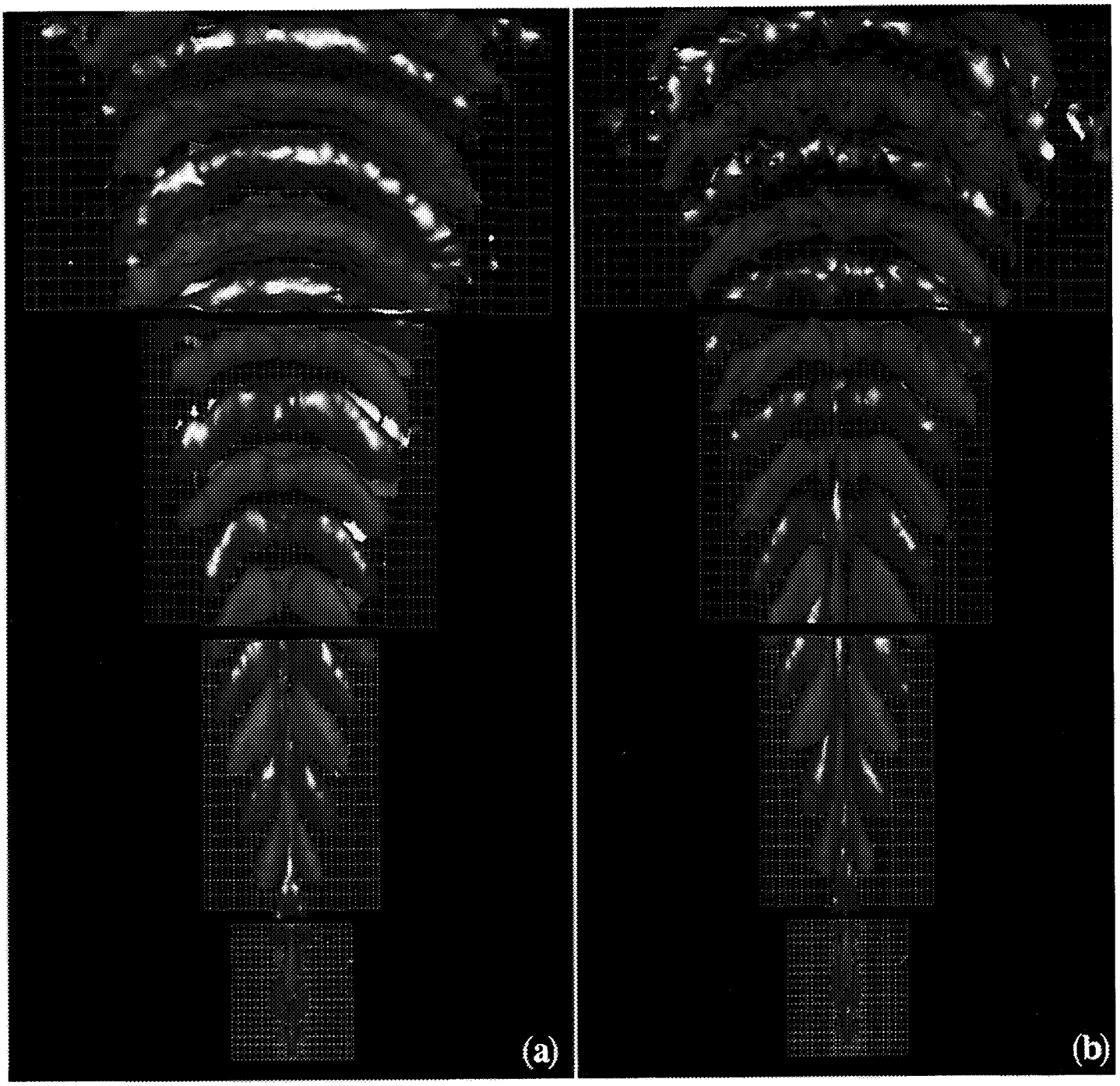

Figure 23. Plan view of TS waves for conditions (a) without suction (b) with suction. Clumping observed downstream for case with suction which could be due to a secondary instabiity associated with suction hole vortices.

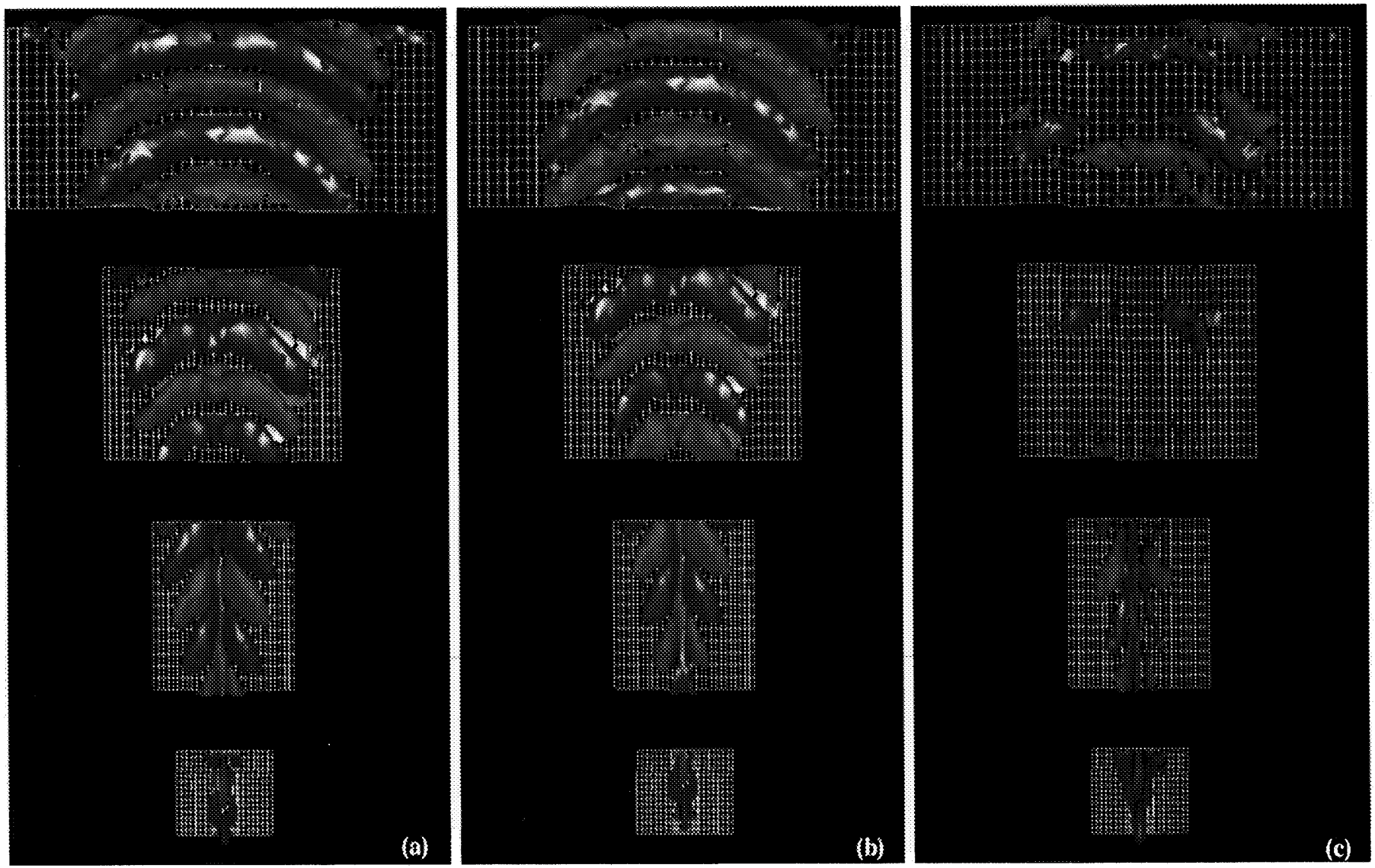

Figure 24. Simulation showing possibility of TS wave cancellation (a) original data (b) original data bodily shifted downstream (c) numerical addition of original and bodily shifted data showing downstream TS wave cancellation.